

Decoding cell signaling via optimal transport and information theory

Mintu Nandi*¹ and Sosuke Ito^{†1,2}

¹Universal Biology Institute, The University of Tokyo, 7-3-1 Hongo, Bunkyo-ku, Tokyo 113-0033, Japan

²Department of Physics, The University of Tokyo, 7-3-1 Hongo, Bunkyo-ku, Tokyo 113-0033, Japan

A central challenge in cellular signal processing is understanding how biochemical networks perform reliably despite molecular noise. Traditionally, mutual information has been widely used to quantify signaling fidelity, capturing how well outputs discriminate distinct input states. However, it fails to capture whether the output also faithfully mirrors the statistical structure of the input, a property crucial in processes like morphogen patterning, dose-dependent signaling, and cellular communication. To address this gap, we introduce the 2-Wasserstein distance from optimal transport theory, which provides a geometric basis for comparing input and output distributions. In our proposed framework, we define mutual information as informational fidelity and the inverse of the 2-Wasserstein distance as geometric fidelity. Applying this dual-fidelity framework to canonical regulatory motifs under Gaussian channel approximation reveals a topology-dependent trade-off: coherent feed-forward loops can achieve high performance in both dimensions, whereas feedback architectures typically sacrifice informational fidelity to enhance geometric fidelity. We demonstrate that theoretical predictions of feedback regulation are well supported by experimental data from tumor necrosis factor signaling. Our results demonstrate that maximizing information alone is not always advantageous and that reliable signaling arises from balancing information transmission with the geometric aspects of signaling. Thus, our analysis establishes geometric fidelity as a fundamental, yet previously unrecognized, dimension of signaling fidelity. It also provides a quantitative, experimentally accessible framework for dissecting natural networks and designing task-specific synthetic circuits.

Introduction

Cells sense, process, and respond to external and internal cues to survive and adapt in a dynamic environment. However, signal transduction processes are challenged by molecular noise, which arises from multiple sources—such as stochastic birth and death of biomolecules, random molecular interactions, and fluctuations in the extracellular environment^{1,2}. These noise sources shape cellular responses and influence the ability of cells to process signals reliably and make accurate decisions^{3,4}. A widely adopted approach to quantify the reliability of signal transmission under noisy conditions is mutual information (MI)^{5–9}. An MI of 1 bit implies that the output can reliably distinguish between two equally likely input states^{9–11}. As MI increases, the system gains higher resolution in distinguishing fine-grained differences in input levels, thus supporting more nuanced and precise cellular decisions^{12,13}. Because of its interpretability, MI has become the standard metric for evaluating signal fidelity in various biological systems^{7,9–11,13}.

However, effective biological functions often require more than just accurate state discrimination. The statistical alignment between input and output distributions (distributional correspondence) can constitute a distinct and critical dimension of performance. Distributional correspondence preserves key structural features of the input, enabling the system to replicate the input characteristics with high fidelity. The biological necessity of such correspondence is evident across systems. For instance, in developmental patterning, morphogen gradients of the Bicoid-Hunchback system in the fruit fly are reproducible across the embryos despite biochemical noise (Fig. 1a)¹⁴. In neuronal networks, input-output consistency plays a

*mintunandi@ubi.s.u-tokyo.ac.jp

†sosuke.ito@ubi.s.u-tokyo.ac.jp

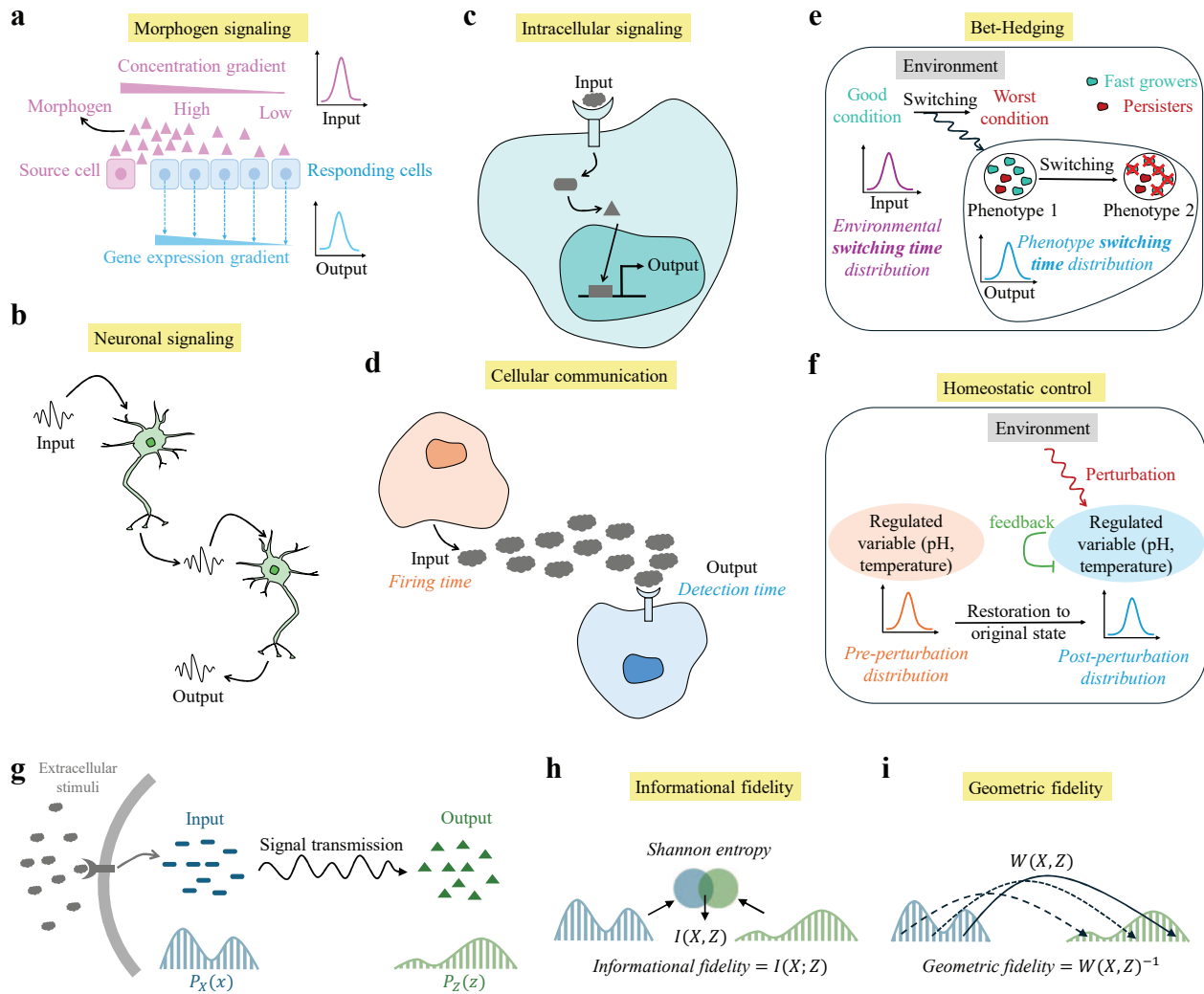


Figure 1. Schematics of signaling systems and the fidelity representations. Illustrative examples of signaling pathways: **a** morphogen signaling, **b** neuronal signaling, **c** intracellular signaling, **d** cell-to-cell communication, **e** bet-hedging, and **f** homeostatic control. **g** A general scheme of signal transduction. Here, the input X acts as an internal representation of the external signals. The input distribution $P_X(x)$ is processed into an output Z with distribution $P_Z(z)$. **h** Informational fidelity is defined as MI between X and Z , $I(X; Z)$. The MI is shown in terms of the overlap of Shannon entropies. **i** Geometric fidelity is defined as the inverse of the 2-WD, $W(X, Z)^{-1}$. The 2-WD $W(X, Z)$ is introduced via an optimal transport problem.

significant role in preserving key input features across several layers of interconnected neurons to reproduce reliable, undistorted output (Fig. 1b)¹⁵. Similarly, several signaling pathways evolve to avoid losing signaling features by transmitting the signal in a linear, undistorted manner^{16,17}. In dose-dependent signaling programs (Fig. 1c), cellular responses scale with input magnitude^{18–21}.

Importantly, the biological meaning of input-output correspondence depends on the variables used to represent inputs and outputs. In signal transduction, these variables are typically the concentration of encoded signaling molecules and the corresponding cellular responses. But in other contexts, different quantities are relevant. For example, in cellular communication channels, signaling accuracy has been previously quantified using MI between the input firing-time and output detection-time distributions of signaling molecules (Fig. 1d)²². In this context, assessing how closely the output distribution preserves the shape of the input distribution can offer complementary insight into the mechanisms that enable reliable and efficient cell-to-cell communication. Moreover, in bet-hedging, the input can be defined as the

distribution of environmental switching times, while the output is the distribution of phenotype switching times (Fig. 1e)²³. Here, optimal performance arises when environmental transition statistics match phenotype transition statistics²³, even though the instantaneous phenotype distribution remains heterogeneous. On the other hand, in homeostatic control, the distributional correspondence is relevant when observed between the pre-perturbation and post-recovery distributions of a regulated variable (Fig. 1f), with effective feedback restoring the original statistical state despite external disturbances^{24,25}. These examples illustrate that input-output correspondence is inherently task-dependent and reflects the functional demands placed on the system. In the present work, we focus on signal transduction, where inputs and outputs correspond to signal and response concentrations, and analyze how distributional correspondence complements MI in characterizing signaling fidelity.

While MI effectively captures how well input states can be distinguished by output, it fails to quantify input-output distributional correspondence. This limitation arises because MI is invariant under invertible transformations of the input or output²⁶. Consequently, MI can identify that a signal was received but cannot determine whether the output distribution preserves the quantitative structure of the input. These observations motivate treating input-output distributional correspondence as a distinct and biologically meaningful dimension of signaling fidelity.

To quantify the input-output correspondence, we introduce the 2-Wasserstein distance (2-WD) from optimal transport (OT) theory²⁷. It quantifies the minimum cost of transforming one probability distribution into another, offering a principled, geometric approach to comparing input and output distributions. In biochemical signaling, where the output is a regulated transformation of the input, the 2-WD value naturally captures how faithfully the input distribution is preserved downstream. A small 2-WD indicates that the output retains key quantitative features of the input, such as its shape, scale (variability), and mean. We note here that recent advances in systems biology have applied OT theory to diverse contexts, such as reconstructing developmental trajectories from single-cell RNA-seq²⁸, aligning multi-omic modalities²⁹, integrating heterogeneous single-cell datasets³⁰, and in neuroscience³¹. Despite these developments, OT remains underutilized in biochemical signal transduction. Given the nonlinear and noisy nature of signaling, the OT-based 2-WD metric can provide a powerful framework for assessing whether cells preserve or distort the output distribution in response to input stimuli.

Building on these perspectives, we integrate OT with information theory to capture the complementary aspects of signal transmission: state resolution and distributional correspondence. We propose that optimal signal transduction is achieved when these two aspects are balanced according to the demands of cellular functions. This implies an inherent trade-off in how cells transmit signals. We consider a general input (X)–output (Z) signaling channel (Fig. 1g) and formulate a theoretical framework where MI, $I(X; Z)$, quantifies informational fidelity—how efficiently the output (Z) encodes the input states (X) (Fig. 1h). Moreover, the inverse of the 2-WD between the input and output distributions, $W(X, Z)^{-1}$, captures geometric fidelity—how closely the output mirrors the input distribution (Fig. 1i). Informational fidelity ignores distributional correspondence, and geometric fidelity alone cannot reliably distinguish input states. This complementarity makes both dimensions essential for a complete description of signal transmission. To apply this framework, we developed gene regulation models that allow for the analytical calculation of MI and the 2-WD across canonical network motifs. This enables us to analyze how regulatory topology shapes cell signaling in the dual-fidelity landscape.

Our results demonstrate that distinct network topologies navigate the trade-off between informational and geometric fidelities in motif-specific ways, revealing diverse signal processing strategies embedded in gene regulatory architectures. Notably, our analysis of experimental data on tumor necrosis factor (TNF) signaling pathway aligns well with the observed motif-specific distinctions. This finding establishes that cells rely on geometric aspects of signaling in addition to state discrimination. Moving beyond conventional approaches that rely solely on MI, our framework unifies the analysis of both dimensions of fidelity and

provides a practical method for studying natural networks and designing synthetic circuits.

Results

The dual-fidelity framework. In order to formalize the framework involving informational and geometric fidelities in signal transduction, we define a variational objective function that integrates MI, $I(X; Z)$ and the 2-WD, $W(X, Z)$ between the input X and the output Z . The objective function is expressed as a Lagrangian of the following form:

$$\mathcal{L} = I(X; Z) - \lambda[W(X, Z)]^2, \quad (1)$$

where λ is a Lagrange multiplier, which captures emergent cellular priorities. We note that λ has units of bits per squared unit of the variable (X or Z) in which $W(X, Z)$ is evaluated. A low λ weights information transmission more heavily, favoring accurate encoding of input states. In contrast, a high λ prioritizes preserving input variability in the output to reflect phenotypic diversity. Thus, λ abstracts the physiological objectives of the cell, distinguishing scenarios that favor state encoding from those that require distributional correspondence. Note that the general form of the Lagrangian \mathcal{L} can be considered the Sinkhorn distance³². It can also be interpreted as the rate-distortion theory²⁶, which has been used in biophysics³³.

We will explain the mathematical definitions of MI and the 2-WD in Eq. (1). MI $I(X; Z)$ is defined as

$$I(X; Z) := \int dx dz P_{X,Z}(x, z) \log_2 \left[\frac{P_{X,Z}(x, z)}{P_X(x)P_Z(z)} \right], \quad (2)$$

where $P_{X,Z}(x, z)$ is the joint distribution of the input and output variables, and $P_X(x) = \int dz P_{X,Z}(x, z)$ and $P_Z(z) = \int dx P_{X,Z}(x, z)$ are the corresponding marginal distributions. The lowercase letters x and z are used to represent the input and output states, respectively, in Euclidean space. Since the base of the logarithm is 2, MI is measured in *bits*. The 2-WD $W(X, Z)$, a geometric measure of dissimilarity between the input distribution $P_X(x)$ and the output distribution $P_Z(z)$, is defined as

$$W(X, Z) := \sqrt{\min_{\pi(x,z) \in \mathbf{\Pi}(P_X, P_Z)} \int dx dz (x - z)^2 \pi(x, z)}, \quad (3)$$

where $\mathbf{\Pi}(P_X, P_Z)$ denotes the set of all joint distributions $\pi(x, z)$ such that the marginals satisfy: $P_X(x) = \int dz \pi(x, z)$ and $P_Z(z) = \int dx \pi(x, z)$ with $\pi(x, z) \geq 0$. Here, $\pi(x, z)$ represents a transport plan. Unlike the true joint distribution $P_{X,Z}(x, z)$, this transport plan is a hypothetical coupling that is only constrained to have the correct marginals $P_X(x)$ and $P_Z(z)$. The function $(x - z)^2$ quantifies the transport cost between two points, and its expected value under the distribution $\pi(x, z)$ represents the total cost of the transport plan. Therefore, the 2-WD indicates the square root of the minimum cost required for transportation, representing the difference in shape between the input distribution P_X and the output distribution P_Z . The 2-WD is a non-negative quantity that yields zero when P_X and P_Z are equal, and satisfies the axioms of a metric²⁷. This 2-WD provides differential geometric and thermodynamic perspectives on the dynamics of the Fokker-Planck equation^{27,34-36}, and these features make it well-suited to the dynamics of the chemical Langevin equation. We note that the 2-WD is expressed in units of X and Z , and that the 2-WD is only meaningful when X and Z are comparable units. Therefore, when using this framework, the units of X and Z must be made equally comparable. For example, in our theoretical analysis, we express X and Z in units of copy numbers, and therefore the 2-WD also has units of copy numbers. In our analysis of the experimental data, we express them in concentration units, and the 2-WD naturally carries the corresponding concentration unit. A detailed interpretation of the meaning of $W(X, Z) = 1$ with appropriate units and its biological implications are also discussed in the *SI text*.

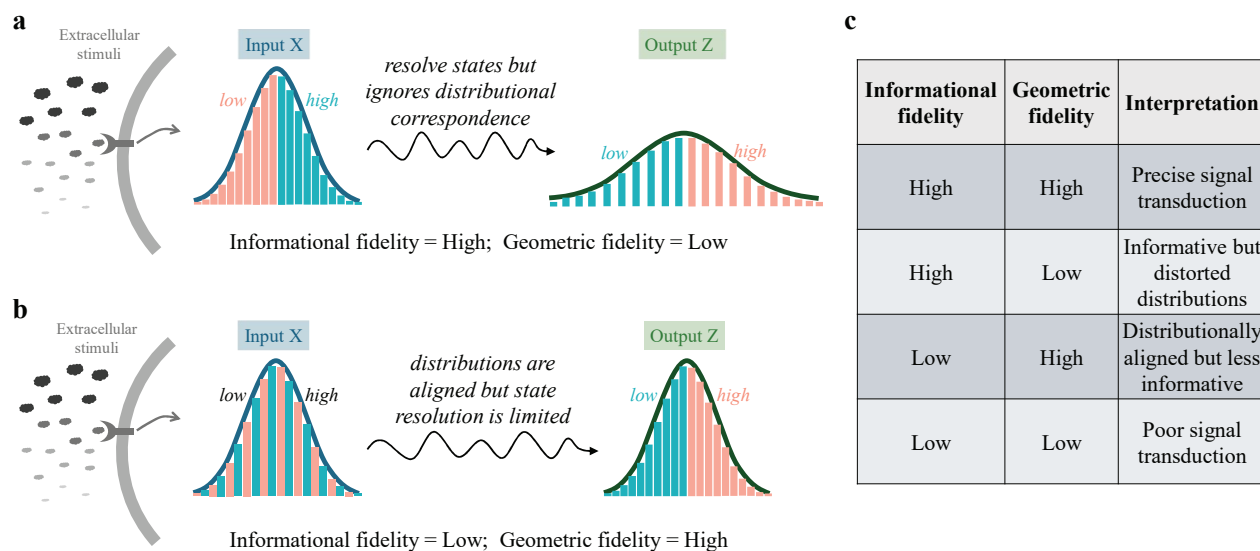


Figure 2. Schematic illustrations of informational and geometric fidelity. **a** Informational fidelity characterizes state-wise mapping between input and output distributions. This mapping resolves states accurately but sacrifices distributional correspondence. **b** Geometric fidelity accounts for shape, scale (variability) and mean-wise mapping of input distribution to output. While this geometric fidelity cannot measure the precise discrimination of input states in the output, it does measure their overall distributional correspondence. **c** A balance between these two fidelities governs cellular decision-making. The table summarizes the various combinations of these two fidelities and their interpretation in signaling.

Significance of dual-fidelity. To understand the biological relevance of the dual-fidelity framework, we connect the two fidelities to the features of signal transduction. High informational fidelity corresponds to accurate state discrimination as illustrated in Fig. 2a. This enables cells to clearly distinguish between input states (e.g., *low* vs. *high*), but it does not capture the correspondence between input and output distributions. Consequently, it fails to account for biological processes requiring such correspondence, such as neuronal networks¹⁵ and many signaling relay pathways^{16,17,37}.

On the other hand, high geometric fidelity corresponds to a mapping of the input distribution into the output, such that peaks, troughs, and overall shape, including variability (scale) and mean of the input distribution are faithfully preserved at the output (Fig. 2b). Unlike informational fidelity, it captures the overall features of the input, but it limits the precise input state discrimination in the output.

Since both fidelities play decisive roles in signal transduction, we propose the dual-fidelity framework as a means to characterize the distinct strategies that biochemical systems adopt for signaling. We hypothesize that the trade-off between these fidelities is fundamental to cellular function. To interpret this trade-off, we summarize how different combinations of the two fidelities correspond to distinct signaling behaviors (see Fig. 2c). When both fidelities are high, signaling is precise, combining accurate state discrimination with distributional correspondence. High informational but low geometric fidelity yields reliable state discrimination but deliberate distributional distortion (illustrated in Fig. 2a). High geometric but low informational fidelity maintains distributional correspondence but weakens state discrimination (illustrated in Fig. 2b). When both are low, signaling is neither informative nor geometrically aligned, indicating poor signal transduction. Thus, neither fidelity alone provides a complete description of signaling; together, they capture the complementary dimensions necessary to elucidate the efficacy of signal transmission. To illustrate this framework, we next analyze canonical gene regulatory motifs using this dual-fidelity framework.

Gene regulation and fidelity optimization. We apply the dual-fidelity framework to six canonical regulatory motifs – simple cascade (SC), coherent type-1 feed-forward loop (C1-FFL), incoherent type-1

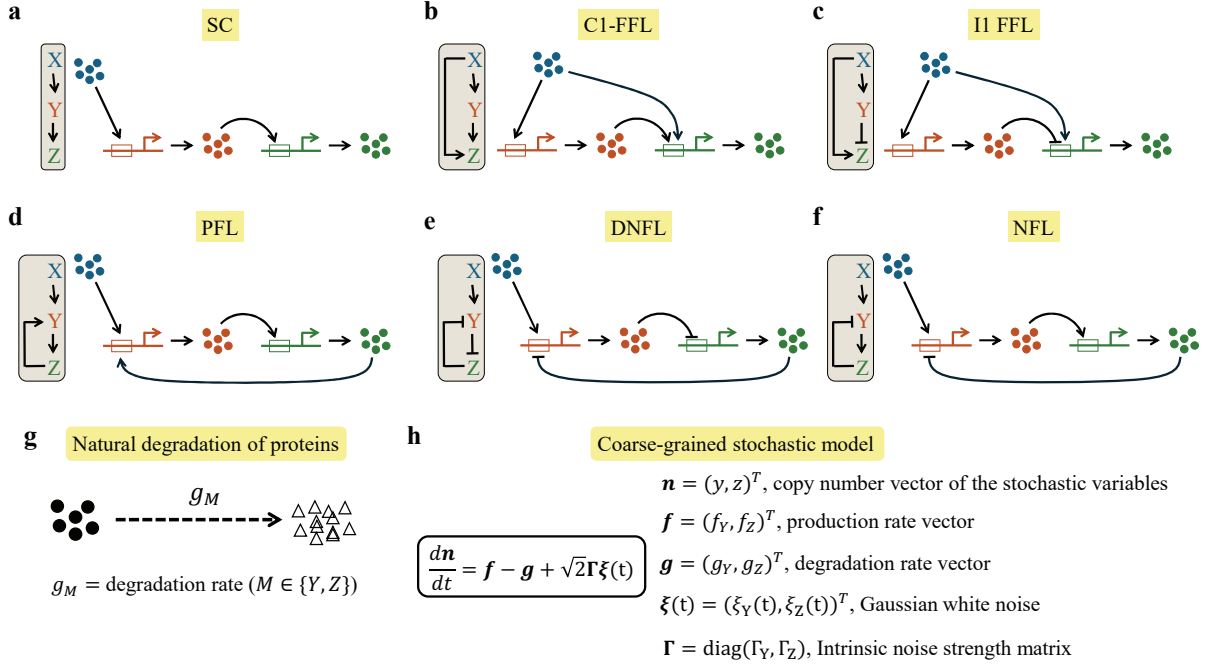


Figure 3. Schematics of gene regulatory motifs and governing dynamical equation. **a** Simple cascade: the input X activates Y , which subsequently activates Z . **b** Coherent type-1 feed-forward loop: X activates both Y and Z , and Y activates Z . **c** Incoherent type-1 feed-forward loop: X activates both Y and Z , but Y represses Z . **d** Positive feedback loop: X activates Y , which again activates Z , and Z activates Y forming the feedback. **e** Double negative feedback loop: X activates Y , which represses Z , and Z represses Y . **f** Negative feedback loop: X activates Y , which again activates Z , but Z represses Y . **g** Natural degradation with rate g_M ($M \in \{Y, Z\}$) is illustrated. **h** The stochastic model for the gene regulatory motifs is shown. Here, $\xi(t)$ denotes the Gaussian white noise satisfying $\overline{\xi_M(t)} = 0$ and $\overline{\xi_M(t)\xi_{M'}(t')} = \delta_{MM'}\delta(t-t')$ with $M \in \{Y, Z\}$ and $M' \in \{Y, Z\}$. The overbar $\overline{\cdot}$ represents the ensemble average.

feed-forward loop (I1-FFL), positive feedback loop (PFL), double negative feedback loop (DNFL), and negative feedback loop (NFL) (Figs. 3a–f). In all cases, proteins degrade at rates \mathbf{g} (Fig. 3g) and are produced according to regulatory functions \mathbf{f} (Fig. 3h). Now, using Gaussian approximations, we analyzed the steady-state behavior of these motifs to study how architecture shapes the fidelity trade-offs.

Stochastic dynamics of the motifs are modeled using coupled differential equations based on the Langevin formalism (see Fig. 3h and [Materials and methods](#)). Solving this equation using linear noise approximation (LNA)^{38,39} yields the following analytical forms for the intensity of the output noise η_Z^2 and the input–output covariance ζ_{XZ} in the steady-state,

$$\eta_Z^2 = \frac{1}{\mu_Z} + \Phi_1 + \Phi_2 \eta_X^2, \quad (4)$$

$$\zeta_{XZ} = \Psi \eta_X^2, \quad (5)$$

where η_X^2 is the intensity of the input noise. The coefficients Φ_1 , Φ_2 , and Ψ depend on system parameters and regulatory sensitivities $f'_{ML} = (\partial f_M / \partial n_L)$ in the steady-state, where f_M (an element of \mathbf{f}) is the production rate in the system $M \in \{Y, Z\}$, and $n_L \in \{x, y, z\}$ is a molecule count (copy number) of the system $L \in \{X, Y, Z\}$. Here f'_{ML} denotes how strongly a gene of the system M is regulated by the system L . The motif-specific forms of f_M and f'_{ML} are provided in the *SI text*.

Among the regulatory sensitivities, we highlight f'_{YX} and f'_{YZ} . These include the dissociation constants K_{XY} and K_{ZY} , which correspond to the binding of X and Z to the promoter of gene Y , respectively (see table in *SI text*). Notably, Z regulates Y only in PFL, DNFL, and NFL, while in SC, C1-FFL, and I1-FFL, Z has no feedback to Y . We now define binding affinity parameters (BAPs) for Y 's promoter as

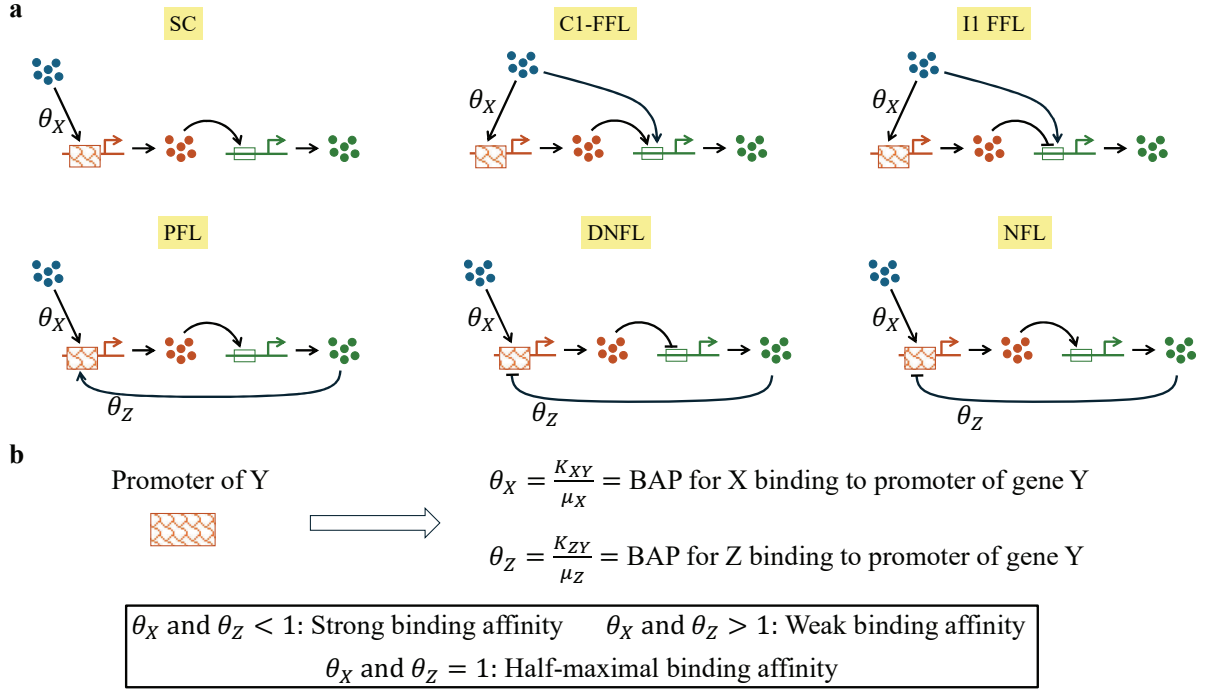


Figure 4. Binding affinity parameters θ_X and θ_Z . **a** Schematic illustration of θ_X and θ_Z across different network motifs. **b** Definition of the binding affinity parameters. θ_X and θ_Z represent the effective binding affinities of X and Z , respectively, to the promoter of gene Y .

$\theta_X = K_{XY}/\mu_X$ and $\theta_Z = K_{ZY}/\mu_Z$ (Fig. 4a), where μ_X and μ_Z denote the steady-state mean copy number of X and Z , respectively. Accordingly, only θ_X is defined for SC, C1-FFL, and I1-FFL motifs, whereas both θ_X and θ_Z are defined for PFL, DNFL, and NFL motifs. A value of $\theta_X < 1$ ($\theta_Z < 1$) implies strong binding affinity of X (Z) to the promoter of Y . $\theta_X > 1$ ($\theta_Z > 1$) denotes weak binding affinity. $\theta_X = 1$ ($\theta_Z = 1$) corresponds to half-maximal binding affinity (Fig. 4b). See *SI text* for detailed discussions.

To facilitate analytical tractability, we adopt Gaussian channel approximations for both MI and the 2-WD (see Eqs. (8) and (10)), allowing us to express these quantities directly in terms of the motif's noise characteristics. This is valid in the steady-state, where copy numbers are kept on the order of hundreds in this study, and the LNA predicts Gaussian fluctuations. The approach provides a principled route to quantify how each regulatory motif balances informational and geometric fidelities under biochemical noise. We note that Eq. (1) defines the general form of dual-fidelity Lagrangian. In practice, both MI and the 2-WD depend on several biochemical parameters. We fix all other biochemical parameters and vary three control variables: the BAPs θ_X and θ_Z , and the Lagrange multiplier λ . For $\theta' \in \{\theta_X, \theta_Z\}$, we consider three regimes: $\theta' < 1$, $\theta' = 1$, and $\theta' > 1$, represented by the values $\theta' = 0.5$, $\theta' = 1$, and $\theta' = 2$, respectively. All nine pairwise combinations of (θ_X, θ_Z) are analyzed for the PFL, DNFL, and NFL motifs, while for SC, C1-FFL, and I1-FFL, only θ_X is varied. The Lagrange multiplier λ can be sampled from a discrete set. With this convention, Eq. (1) takes the parameterized form $\mathcal{L}(\eta_X^2; \theta_X, \theta_Z, \lambda)$ when the set of parameters $(\eta_X^2, \theta_X, \theta_Z, \lambda)$ is fixed. For varying combinations of (θ_X, θ_Z) and different values of λ , we evaluate the optimal input noise η_X^{2*} , via

$$\eta_X^{2*} = \arg \max_{\eta_X^2} \mathcal{L}(\eta_X^2; \theta_X, \theta_Z, \lambda), \quad (6)$$

We note that Eq. (6) applies to both the set of motifs $\{\text{SC, C1-FFL, I1-FFL}\}$ and $\{\text{PFL, DNFL, NFL}\}$, where θ_Z dependence is absent for the former set (see Fig. 4a). We treat the input noise, η_X^2 , as a variational parameter to reflect upstream variability that is extrinsic to the downstream components in

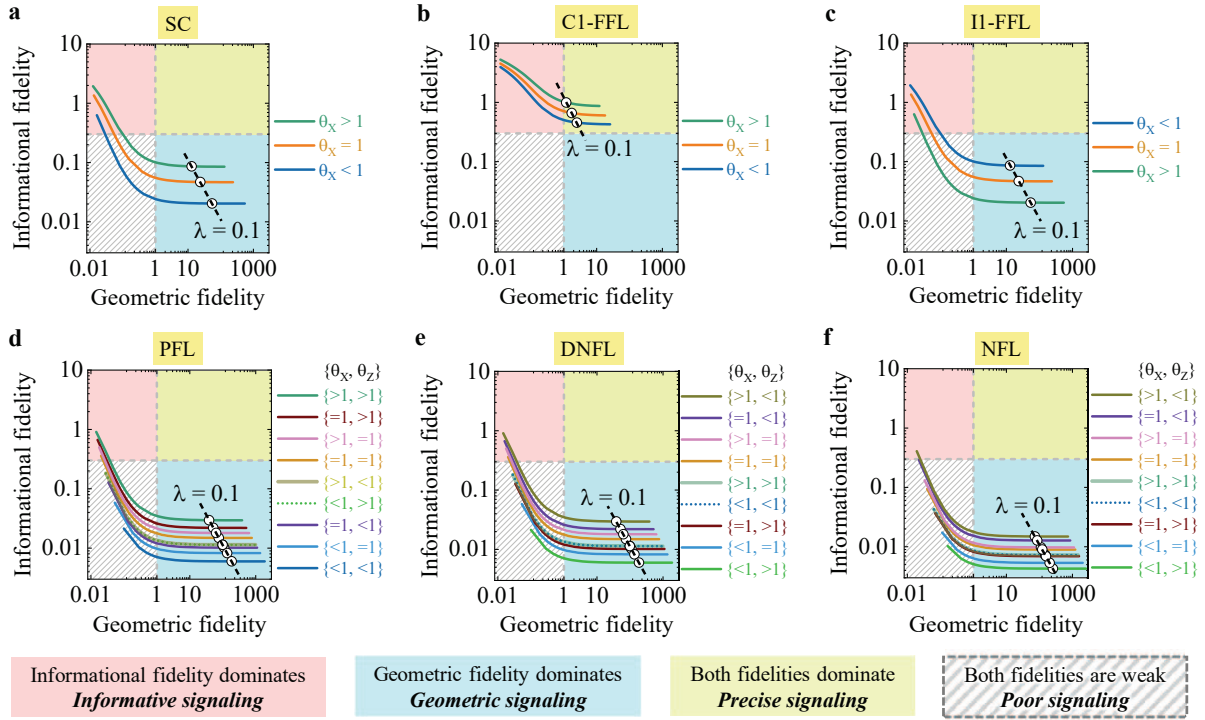


Figure 5. Trade-off between informational and geometric fidelities across network motifs. The relationships between the two fidelities obtained from the dual-fidelity optimization framework for six canonical motifs: **a** Simple cascade, **b** Coherent type-1 feed-forward loop, **c** Incoherent type-1 feed-forward loop, **d** Positive feedback loop, **e** Double negative feedback loop, and **f** Negative feedback loop. Each curve represents how the operating regime shifts as BAP and λ are varied. The model parameters used to generate these plots are mentioned in *SI text*.

the gene regulatory network. This choice mirrors many biological scenarios where the input signal arises from external or upstream sources, such as extracellular ligands or environmental fluctuations, and is not subjected to internal regulation. Optimizing over η_X^2 thus enables us to explore how each network architecture transforms varying degrees of input variability into output responses, and how it balances the competing demands of state encoding and distributional correspondence. The parameters λ and BAPs are key determinants governing this trade-off. While λ dictates the physiological context of the cell and sets the priority accordingly, BAPs control the gene expression of Y through regulation by X and/or Z . These regulatory differences shape the role of Y in signal processing and influence the dual-fidelity trade-offs accordingly.

Fidelity trade-offs due to differential binding affinities. Using Eq. (6), we compute the optimal input noise η_X^{2*} for each motif in Figs. 3a-f across different combinations of BAPs and different values of λ . The corresponding output noise η_Z^2 and input-output covariance ζ_{XZ} follow from Eqs. (4)–(5), which determine MI and the 2-WD via Eqs. (8) and (10). In these calculations, we fix the mean copy numbers of X , Y , and Z to be equal (see *SI text*) to isolate the effect of input variability. The resulting trade-offs between informational and geometric fidelity are shown in Fig. 5, with each curve representing a specific binding affinity profile over varying λ .

We now analyze the effect of binding affinity at $\lambda = 0.1$ across all motifs. Each motif exhibits a distinct hierarchy as BAPs vary. In SC, weak binding of X ($\theta_X > 1$) increases informational fidelity but decreases geometric fidelity, while strong binding ($\theta_X < 1$) produces the opposite (Fig. 5a). Weak binding leaves Y 's promoter largely unoccupied, so small fluctuations in X strongly modulate occupancy and output. This amplifies the absolute value of the input–output covariance ($|\zeta_{XZ}|$), boosting informational fidelity, but also inflates output noise (η_Z^2), reducing geometric fidelity (as is directly evident from Eqs. (8) and (10)). Strong

binding saturates the promoter, damping Z variability and improving geometric fidelity, but lowering $|\zeta_{XZ}|$ and informational fidelity. C1-FFL shows a similar trend with different magnitudes, reflecting its coherent topology where both arms activate Z ^{40,41} (Fig. 5b).

In contrast, I1-FFL inverts the pattern (Fig. 5c): one branch activates and the other represses Z ⁴², so strong binding in one arm can offset fluctuations in the other, reducing variability without saturation. PFL follows SC/C1-FFL: weak binding of both X and Z ($\theta_X > 1$, $\theta_Z > 1$) yields high informational fidelity but low geometric fidelity, while strong binding of both does the reverse. Intermediate affinities produce intermediate outcomes (Fig. 5d). DNFL and NFL behave similarly to each other but differ from the other motifs. In both, weak X binding combined with strong Z binding increases variability and favors informational fidelity at the cost of geometric fidelity, while the reverse (strong X , weak Z) stabilizes Y , lowering informational fidelity but improving geometric fidelity. The difference in magnitude between DNFL and NFL arises from the specific regulatory effect of Z on Y .

Overall, these results highlight that the trade-off is shaped by how binding affinities of Y 's promoter modulate through each network topology. Coherent architecture tends to align in its response to affinity changes, whereas incoherent and feedback-containing motifs can invert or alter this trend due to opposing regulatory effects. Such patterns suggest that cells could exploit binding affinity tuning as a versatile mechanism to balance informational and geometric fidelities according to functional demands. Next, we examine the relative motif-specific preferences for the two fidelities.

Motif-specific patterns in dual-fidelity space. To compare motif performances, we map their trade-off curves into four qualitative regimes: informative, geometric, precise, and poor signaling. The regime boundaries are chosen for interpretability and are not strict cutoffs. We choose $I(X; Z) \geq 0.3$ bits as the minimum for biologically meaningful state discrimination¹⁰, and $W(X, Z)^{-1} \geq 1$ in (copy numbers)⁻¹ unit as the minimum for reliable distributional correspondence (explicitly discussed in *SI text*). Based on this classification, informative signaling corresponds to $I(X; Z) \geq 0.3$ bits with $W(X, Z)^{-1} < 1$, geometric to $I(X; Z) < 0.3$ bits with $W(X, Z)^{-1} \geq 1$, precise to $I(X; Z) \geq 0.3$ bits with $W(X, Z)^{-1} \geq 1$, and poor to $I(X; Z) < 0.3$ bits with $W(X, Z)^{-1} < 1$. These regimes provide a convenient framework for comparing motif topologies in the dual-fidelity landscape.

In the dual-fidelity space, SC and I1-FFL span a broad range, accessing informative, geometric, and poor signaling regimes (Figs. 5a,c). C1-FFL is largely confined to informative and precise regimes (Fig. 5b), consistent with its role in sustaining coordinated responses for robust signal transmission^{40,41}. Feedback motifs (PFL, DNFL, NFL) primarily explore geometric and poor signaling regimes, with limited access to informative signaling. Among them, NFL shows the strongest bias toward geometric fidelity (Figs. 5d-f). These trends highlight how network structure biases the balance between state resolution and distributional correspondence.

Observed preferences within the dual-fidelity space are qualitatively consistent with reported motif abundances in natural networks. In *Escherichia coli* and yeast transcription networks, C1-FFL and I1-FFL are the most frequent motifs⁴¹⁻⁴⁴. We hypothesize that the prevalence of C1-FFL may stem from its capacity for high information transmission and access to precise signaling regimes. Conversely, the abundance of I1-FFL might be predicted by its unique versatility across varied fidelity modes. In developmental transcription networks, motifs such as SC, PFL, and DNFL are notably enriched. Our model suggests this may be advantageous due to SC's long-timescale operation and fidelity flexibility, while PFL and DNFL might be favored where stability via high geometric fidelity is a primary evolutionary constraint. Furthermore, the rarity of the NFL in transcriptional networks—often restricted to hybrid regulatory systems⁴⁵—aligns with our prediction of its low information transmission capacity (informational fidelity $\ll 1$) compared to PFL and DNFL, which can approach ~ 1 bit under suitable BAP (Figs. 5d-f).

These observations suggest a design principle for motif organization: (1) C1-FFL achieves high informational fidelity and also retains strong geometric fidelity in the precise regime, (2) I1-FFL provides tunable

shaping of responses, with moderate cost to distributional correspondence, (3) Feedback motifs prioritize geometric fidelity for stability, sacrificing information to some extent. Binding affinity tuning shifts motifs along this fidelity spectrum, providing a biochemical lever to match network performance to functional demands.

Experimental signature of dual-fidelity trade-offs. We analyze single-cell measurement data of nuclear factor- κ B (NF- κ B) and activating transcription factor-2 (ATF-2) responses to TNF stimulation (Fig. 6a), as reported by Cheong *et al.*¹⁰. This study provides dose-response statistics for thousands of mouse fibroblast cells exposed to varying TNF concentrations for 4 hours, in wild-type (WT) cells and A20-deficient (A20^{-/-}) mutant cells. The dose-response statistics report the mean concentrations (in a.u.) and the corresponding standard deviations (in a.u.) of NF- κ B and ATF-2 for both cell types. In WT cells, A20 mediates a negative feedback to the TNF pathway, whereas this regulation is absent in the A20^{-/-} mutant. We assign TNF as the input X and either NF- κ B or ATF-2 as the output Z , depending on the pathway analyzed (Fig. 6a). Using the reported dose-response statistics, we reconstruct the joint distributions of X and Z and their corresponding marginals to reproduce the reported MI values between TNF and each output for both cell types¹⁰. From the reconstructed marginal distributions, we quantify the corresponding geometric fidelity for both WT and A20^{-/-} cells. We summarize the quantities measured for each cell type and pathway in Fig. 6b, which links each experimental condition to the corresponding pair of fidelity measures. See [Materials and methods](#) for further details.

In Fig. 6c, we plot the measured informational and geometric fidelities for each experimental condition (summarized in Fig. 6b), which shows a distinct separation between WT and A20^{-/-} cells in the dual-fidelity space. For the NF- κ B pathway, deletion of A20 shifts cells toward higher informational fidelity but lower geometric fidelity compared to WT cells (Fig. 6c). This trade-off arises from the role of A20-mediated negative feedback. In WT cells, this feedback suppresses both maximum inducible NF- κ B responses (dynamic range) and noise across all TNF concentrations (Fig. 6d). The dynamic range, here, is measured as the difference in mean concentrations of NF- κ B at the highest and lowest TNF concentrations. The noise level is quantified as the coefficient of variation, defined as the ratio of the standard deviation of the single-cell NF- κ B concentration distribution to the corresponding mean concentration at each TNF dose. Both the mean and standard deviation values used for these calculations are extracted from the dose-response data reported in Cheong *et al.*¹⁰ and are reproduced in the *SI text*. The suppression in the dynamic range and noise in the WT cells limits the distinguishability of TNF states, thereby reducing informational fidelity, but enhances geometric fidelity by maintaining correspondence between TNF and NF- κ B distributions. In contrast, A20^{-/-} cells lack this regulatory buffering, causing NF- κ B responses to exhibit a broader dynamic range and significantly higher noise (Fig. 6d). This allows for better discrimination of different TNF levels, thereby enhancing informational fidelity, but sacrifices the correspondence between TNF and NF- κ B distributions, resulting in reduced geometric fidelity.

Interestingly, the ATF-2 pathway, although not directly regulated by A20, shows a similar but less pronounced effect. Because ATF-2 and NF- κ B share the upstream TNF-receptor complex, changes in NF- κ B dynamics can indirectly affect ATF-2 activation. We note that, similar to NF- κ B, the dynamic range and noise for ATF-2 responses are quantified from the mean concentration and standard deviation values extracted from Cheong *et al.*¹⁰ and reproduced in the *SI Text*. Compared to WT cells, A20 deletion also results in increased noise and dynamic range in ATF-2 (Fig. 6d), shifting the A20^{-/-} cells toward higher informational and lower geometric fidelities in the dual-fidelity space (Fig. 6c). Thus, both NF- κ B and ATF-2 exhibit consistent shifts in the dual-fidelity space upon loss of A20 feedback. These observations suggest that even indirect modulation through shared upstream pathways can influence dual-fidelity trade-offs in downstream effectors.

Importantly, these results highlight the limitations of interpreting signal transmission solely in terms of informational fidelity. Based only on information transmission, one might conclude that the A20^{-/-}

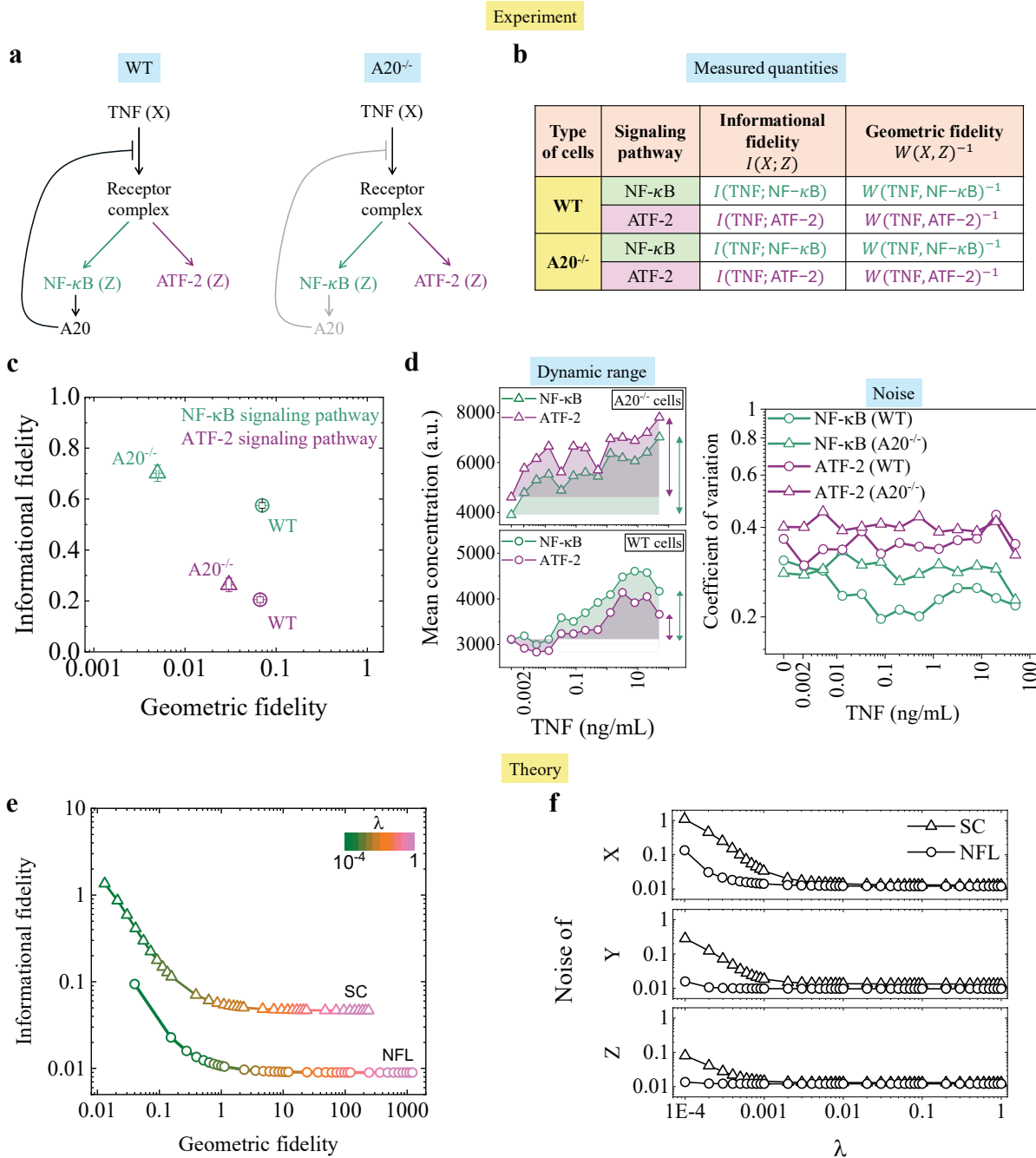


Figure 6. Theory-experiment correspondence of dual-fidelity trade-offs. **a** Schematic of TNF signaling in wild-type (WT) cells and A20-deficient (A20^{-/-}) mutant cells. **b** Summary of measured quantities: informational fidelity $I(X; Z)$ and geometric fidelity $W(X, Z)^{-1}$ for NF- κ B and ATF-2 pathways in both WT and A20^{-/-} cells. **c** Informational fidelity is plotted against geometric fidelity, using the quantities summarized in **b**. The detailed method of estimating the two fidelities is given in *SI text*. Informational fidelity is expressed in *bits* and the geometric fidelity in the unit reciprocal to that of TNF concentration. **d** Dynamic range (indicated by arrows) and noise at all TNF concentrations. We quantify noise by the coefficient of variation, defined as the ratio of standard deviation to the mean concentration. These plots are generated from the reported dose-response statistics¹⁰. See *SI text* for further details. **e** Trade-off curves for simple cascade with $\theta_X = 1$ and negative feedback loop with $\theta_X = 1$ and $\theta_Z = 1$, across different values of λ . These plots are reproduced from Figs. 5a and 5f. Here, the informational fidelity is also expressed in *bits*, but the geometric fidelity has the unit reciprocal to the copy numbers (units of X and Z). **f** Optimal noise (η_L^{2*}) of X , Y , and Z for SC and NFL motifs with same BAPs. The optimal noise values are obtained from Eq. (6).

mutant performs better than WT, since it exhibits higher informational fidelity about the input TNF levels. However, this interpretation from only an information processing perspective contradicts the notion that WT cells represent an evolutionarily optimized state. This contradiction becomes comprehensible only by introducing the concept of geometric fidelity. From this perspective, WT has been optimized not only for transmitting information but also for preserving geometric fidelity, ensuring proportional and stable signal-response relationships. In contrast, A20 deficiency enhances information transmission at the cost of losing geometric fidelity, breaking the balance established by feedback regulation. Crucially, this means WT cells are optimized from the dual perspectives of geometric and informational fidelities, whereas A20^{-/-} cells disrupt this optimization due to the absence of feedback control.

The experimental separation between with-feedback (WT) and without-feedback (A20^{-/-}) cell types in Fig. 6c closely follows the theoretical trends. To illustrate the correspondence between theory and experiment, we reproduced the theoretical curves in Fig. 6e from Figs. 5a and 5f for the two motifs: the SC (with $\theta_X = 1$) which lacks feedback and the NFL (with $\theta_X = 1$ and $\theta_Z = 1$) which contains the negative feedback. We note that in the experiment, geometric fidelity is expressed in the unit reciprocal to TNF concentration, while in the theory, it is expressed in the unit reciprocal to copy number. Hence, absolute magnitudes are not directly comparable; rather, we compare the trends and separations. Although the model topologies differing from the biochemical details of TNF–NF- κ B/ATF-2 network, both the experimental and theoretical results display a consistent qualitative picture – negative feedback shifts signaling toward higher geometric fidelity and lower informational fidelity, whereas the absence of feedback produces the opposite trend. In the theoretical analysis, this trade-off arises because NFL suppresses noise in all gene products (X , Y , and Z) relative to SC (Fig. 6f), thereby maintaining correspondence between input-output distributions but reducing state resolution. Here, the noise of X , Y , and Z refer to the optimal noise levels of these gene products. To be specific, the optimal noise of X , η_X^{2*} , for SC and NFL are calculated from Eq. (6), whereas the optimal noise of Y (η_Y^{2*}) and Z (η_Z^{2*}) are computed from their analytical expressions in terms of the noise intensity of X , as provided in the *SI text*. It should be noted that these theoretical noise intensities are quantified by the squared coefficient of variation, defined as variance divided by the squared mean.

However, the experimental noise in Fig. 6d is quantified by the coefficient of variation. The mean concentration and standard deviation values, used to compute this quantity, were obtained from single-cell fluorescence measurements reported in Cheong *et al.*¹⁰. Here, NF- κ B and ATF-2 fluorescence intensities were measured in arbitrary units (a.u.) and serve as proxies for molecular concentrations. For each TNF concentration, the experiment recorded these fluorescence intensities from thousands of cells and yielded concentration distribution of the outputs. The mean concentration, therefore, represents the average fluorescence intensity across the cell population, and the standard deviation captures how much individual cells deviate from that mean. These experimental values, therefore, represent ensemble statistics of the cell population (see [Materials and methods](#)). Thus, both the noise measurements in theory and experiment represent normalized fluctuations around the mean and capture comparable notions of variability. The underlying correspondence between experimental and theoretical observations, thus, indicates that the balance between information transmission and distributional correspondence is a general feature, regardless of the specific biochemical details.

Discussion

We introduce two complementary fidelity measures in signal transduction, geometric and informational fidelity, based on optimal transport and information theory. The informational fidelity is quantified by MI and is a widely explored concept in the context of cellular information processing^{5,9-12}. It captures how well an output response of a cell can discriminate between distinct states of the input in the presence of noise, but does not inform about input-output distributional correspondence, which is beneficial for

diverse biological systems¹⁴⁻²⁵. On the other hand, the geometric fidelity, quantified by the inverse of the 2-WD, evaluates how faithfully the output preserves the statistical features of the input, but cannot resolve distinct input states accurately. These limitations make the two measures complementary in the context of signal transduction. We therefore propose the dual-fidelity framework to address the distinct strategies that biological systems adopt for efficient signaling.

We apply this dual-fidelity framework to canonical gene regulatory motifs and show that network topology and biochemical parameters govern a fundamental trade-off between informational and geometric fidelities. We find that the C1-FFL emerges as a superior architecture for achieving both informative and precise signaling, consistent with its role as a robust signal encoder^{40,44}. In contrast, feedback architectures, particularly the NFL, prioritize geometric fidelity at the expense of information transmission, ensuring that output remains stable and precisely tracks the input distribution, in accordance with their known role in buffering cellular responses^{46,47}. Thus, circuit topology enables cells to meet distinct physiological demands by balancing state discrimination with distributional correspondence and ensuring robust signaling. This capacity is further tuned by biochemical parameters such as promoter binding affinities, which act as molecular levers shifting network performance within the dual-fidelity space.

Our experimental analysis of the TNF signaling pathway supports the theoretical prediction for negative feedback. We observe that removal of the A20-mediated negative feedback in the TNF signaling pathway shifts the system toward higher informational fidelity but lower geometric fidelity compared to WT cells. This does not indicate a superior design; rather, it reflects the same trade-off observed in theory, where feedback circuits maintain distributional correspondence at the cost of information transmission. Physiologically, negative feedback serves to constrain variability, prevent overactivation, and coordinate multiple downstream pathways, roles that depend on geometric fidelity. From this perspective, the higher informational fidelity in A20-deficient cells arises not as an advantage but as a result of feedback loss. However, interpreting signal transmission solely through information transmission can be misleading. In this perspective, A20^{-/-} cells would seem to outperform WT, contradicting the idea that WT represents an evolutionarily optimized state. This apparent paradox is resolved by considering geometric fidelity, which clarifies that WT signaling has evolved to maintain a balance between informational and geometric fidelity. These results challenge the notion that maximizing information transmission is always advantageous.

More broadly, our framework refines the conceptual understanding of signaling fidelity by revealing that information transmission alone cannot fully capture optimal signaling performance; geometric fidelity provides an essential complementary dimension that explains the evolutionary tuning of signaling networks. Moreover, the agreement between experimental and theoretical results shows that the trade-off between information transmission and distributional correspondence predicted by our model is realized in actual cellular context. Thus, our dual-fidelity framework provides a clear quantitative link between theory and experiment, connecting network topology with measurable signaling behavior.

Our theoretical findings are based on the Gaussian approximations, which allow us to evaluate MI and the 2-WD directly from means and covariances (Eqs. (8) and (9)). Such analytical tractability enables direct exploration of the trade-offs without resorting to numerical computations. While the Gaussian framework captures many biologically relevant regimes, the distributions often deviate due to gene expression bursting or multi-stability. Extending the dual-fidelity framework to these cases would require computing MI from the full joint distribution (Eq. (2)), and evaluating the 2-WD from its general optimal transport formulation (Eq. (3)), typically necessitating numerical methods. Given the channel $P(z|x)$ is well approximated as a Gaussian channel, MI is maximized by a Gaussian input distribution $P_X(x)$ for fixed covariance. Under this assumption, the MI computed within Gaussian approximation, denoted $I_{\text{Gaussian}}(X; Z)$, provides an upper bound on the true informational fidelity achievable by any input distribution with the same covariance, i.e., $I_{\text{Gaussian}}(X; Z) \geq I(X; Z)$ ²⁶. In contrast, the 2-WD admits a lower bound, where the Gaussian input and output distributions with given means and co-

variances minimize the 2-WD⁴⁸. Consequently, the 2-WD computed within the Gaussian distribution $W_{\text{Gaussian}}(X, Z)$ satisfies $W_{\text{Gaussian}}(X, Z) \leq W(X, Z)$, and hence the corresponding geometric fidelity satisfies $W_{\text{Gaussian}}(X, Z)^{-1} \geq W(X, Z)^{-1}$. Combining these two bounds, the Gaussian evaluated Lagrangian $\mathcal{L}_{\text{Gaussian}} := I_{\text{Gaussian}}(X; Z) - \lambda[W_{\text{Gaussian}}(X, Z)]^2$ provides an upper bound on the true objective \mathcal{L} for fixed means and covariances, under the Gaussian channel approximation. Therefore, within this regime, our Gaussian analysis yields an upper bound on the achievable dual-fidelity trade-off, and the qualitative conclusions drawn from it remain valid. When $P(z|x)$ deviates substantially from a Gaussian form, however, no general upper bound on $I(X; Z)$ and hence on \mathcal{L} is guaranteed, motivating numerical evaluation using full distributions.

According to the analogy of thermodynamic trade-off relations^{35,49}, the 2-WD-based Lagrangian \mathcal{L} can provide a universal lower bound for various other objective functions in the rate-distortion theory. The 2-WD is related to the 1-Wasserstein distance $W_1(X, Z)$, which is given by the dual optimization problem (Kantorovich-Rubinstein duality²⁷), and it is known that the inequality $W(X, Z) \geq W_1(X, Z) \geq \int dx dz (h(x) - h(z)) P_{X,Z}(x, z) =: D_h(X, Z)$ holds for any observable h satisfying the 1-Lipschitz condition $\|\nabla h\| \leq 1$. Therefore, the inequality $\mathcal{L}_h \geq \mathcal{L}$ always holds for the objective function $\mathcal{L}_h := I(X; Z) - \lambda[D_h(X, Z)]^2$ using other distortions $[D_h(X, Z)]^2$. This implies that the behavior can be similar to that observed with \mathcal{L} even when using a different objective function \mathcal{L}_h to describe changes in distribution. This suggests that our result could be robust to differences in various definitions for the distribution changes.

Beyond understanding signaling reliability, our framework provides a practical tool for experimental and computational researchers. Because geometric fidelity relies on distributional statistics, it can be computed from the fluorescence intensity data of both single-cell and cell population experiments. Observed signaling responses can be mapped onto this space to infer prioritization of state discrimination versus distributional correspondence and to diagnose underlying regulatory architectures. Thus, our approach not only advances theory but also supplies a quantitative lens that experimental and modeling communities can use to interrogate signaling fidelity in diverse biological systems.

Furthermore, our framework offers a practical guide for designing synthetic regulatory circuits tailored to specific demands. Our results suggest that tuning transcription factor binding affinities provides a direct means of controlling the trade-off between informational and geometric fidelity. Circuits designed to faithfully reproduce the quantitative features of the input can be optimized for high geometric fidelity and low informational fidelity by adjusting the binding affinity parameter. Conversely, circuits intended for decision-making can be constructed by achieving high informational fidelity and low geometric fidelity by tuning the binding affinity parameter. Beyond binding affinities, additional control over this trade-off can be achieved by tuning the production and degradation rates of regulatory components^{50–52}. Thus, our dual-fidelity approach serves as a design framework for synthetic biologists to engineer robust, task-specific synthetic circuits.

In summary, our study reveals that maximizing information alone is not always advantageous; rather, a balance between information transmission and distributional correspondence is more fundamental to reliable signaling. By formalizing this balance, this work establishes geometric fidelity, via the 2-WD, as a fundamental and previously unrecognized dimension of signaling fidelity, placing OT theory alongside information theory in the quantitative study of cell signaling.

Materials and methods

Modeling genetic interactions. The stochastic dynamics of each network are governed by the Langevin equation shown in Fig. 3h, with the copy number vector $\mathbf{n} = (y, z)^\top$ and degradation rate vector $\mathbf{g} = (g_Y, g_Z)^\top$, where \top denotes the vector transpose (motif-specific forms are tabulated in *SI text*). Although the dynamical form remains the same across networks, the regulatory structure is encoded in the production rate vector $\mathbf{f} = (f_Y, f_Z)^\top$, which varies with topology. f_M ($M \in \{Y, Z\}$) is modeled using Hill-type

functions for both activation and repression (see *SI text*), and transcription factor binding dynamics are coarse-grained into its effective nonlinearities for analytical tractability. The steady-state mean levels are denoted by μ_M . All copy numbers are dimensionless and represent absolute molecule counts.

To account for intrinsic molecular fluctuations, we adopt a stochastic framework for Y and Z , and the input X is modeled as a Gaussian-distributed non-dynamical (static) random variable, $x \sim \mathcal{N}(\mu_X, \sigma_X^2)$, with mean μ_X and variance σ_X^2 . The dynamics of Y and Z follow Langevin-type differential equations (see Fig. 3h) of the form^{53–58},

$$\frac{d\mathbf{n}}{dt} = \mathbf{f} - \mathbf{g} + \sqrt{2}\mathbf{\Gamma}\boldsymbol{\xi}(t), \quad (7)$$

where $\boldsymbol{\xi}(t) = (\xi_Y(t), \xi_Z(t))^\top$ denotes a Gaussian white noise vector satisfying $\overline{\xi_M(t)} = 0$ and $\overline{\xi_M(t)\xi_{M'}(t')} = \delta_{MM'}\delta(t-t')$ with $M \in \{Y, Z\}$ and $M' \in \{Y, Z\}$. Here, the overbar $\overline{\dots}$ is used to denote the expectation value. The statistical properties imply that the noise processes are temporally uncorrelated and independent across species^{38,59–63}. We write the stochastic term as $\sqrt{2}\mathbf{\Gamma}\boldsymbol{\xi}(t)$, where $\mathbf{\Gamma} = \text{diag}(\Gamma_Y, \Gamma_Z)$ is a noise-amplitude matrix. With this convention, the corresponding diffusion matrix in the associated Fokker-Planck description is $\mathbf{D} = \mathbf{\Gamma}\mathbf{\Gamma}^\top$. Due to LNA, $\mathbf{D} = \text{diag}(D_Y, D_Z)$ at steady-state is given by $D_Y = [f_Y(\mu_X, \mu_Z) + g_Y(\mu_Y)]/2$ and $D_Z = [f_Z(\mu_X, \mu_Y) + g_Z(\mu_Z)]/2$ ⁶¹, where $f_Y(\mu_X, \mu_Z)$ and $f_Z(\mu_X, \mu_Y)$ denote the production rates of Y and Z , respectively, and $g_Y(\mu_Y)$ and $g_Z(\mu_Z)$ represent corresponding degradation rates, evaluated in the steady-state (see *SI text*).

We apply the LNA^{38,39} to Eq. (7) to derive analytical expressions for the statistical moments associated with each variable in the steady-state (see *SI text*). This approach is valid in the mesoscopic regime (molecule count \sim hundreds)^{7,62}, where the Langevin framework approximates the chemical master equation and yields the covariance matrix upon LNA^{38,39,58–60}. The noise in copy numbers of L is introduced as $\eta_L^2 = \sigma_L^2/\mu_L^2$ and $\zeta_{LL'} = \sigma_{LL'}/(\mu_L\mu_{L'})$ ($L \in \{X, Y, Z\}$ and $L' \in \{X, Y, Z\}$), where σ_L^2 and $\sigma_{LL'}$ denote the variance and covariance, and μ_L corresponds the mean values in the steady-state. Here η_L^2 denotes the squared coefficient of variation (CV^2) and $\zeta_{LL'}$ represents the normalized covariance. These quantities form the basis of our analytical calculations of MI and the 2-WD.

MI and the 2-WD under Gaussian approximation. Under Gaussian channel approximation with Gaussian input, MI can be analytically characterized using properties of multivariate normal distribution as⁶⁴,

$$I(X; Z) = \frac{1}{2} \log_2 \left(\frac{\eta_X^2 \eta_Z^2}{\eta_X^2 \eta_Z^2 - \zeta_{XZ}^2} \right). \quad (8)$$

We note that MI is generally defined in terms of variances and covariances^{26,65}, we express it here in terms of CV^2 to explicitly connect information transmission to molecular noise, providing a noise-centric view of information transmission.

The 2-WD between marginally Gaussian X and Z is given by⁴⁸,

$$W(X, Z) = \sqrt{(\mu_X - \mu_Z)^2 + (\sigma_X - \sigma_Z)^2}. \quad (9)$$

Substituting $\sigma_L = \mu_L \eta_L$, this becomes,

$$W(X, Z) = \sqrt{\mathcal{V}_X + \mathcal{V}_Z - 2\mathcal{C}_{XZ}}, \quad (10)$$

where, $\mathcal{V}_X = (1 + \eta_X^2)\mu_X^2$, $\mathcal{V}_Z = (1 + \eta_Z^2)\mu_Z^2$, and $\mathcal{C}_{XZ} = \left(1 + \sqrt{\eta_X^2 \eta_Z^2}\right)\mu_X \mu_Z$. These closed-form expressions, Eqs. (8) and (10), enable us to evaluate MI and the 2-WD directly from steady-state means and noise, allowing a quantitative comparison of informational and geometric fidelities across network architectures.

Processing and analysis of experimental data. We analyze single-cell data of the TNF—NF- κ B (TNF—ATF-2) signaling network, measured in thousands of individual mouse fibroblast cells for WT and A20^{-/-} cell types (Fig. 6a), reported in Cheong *et al.*¹⁰. The authors analyzed information transmission capacity of the TNF signaling pathways at 30 min and 4 hours post TNF stimulation. Here, we exclusively focused on the 4-hour dataset because at this long time limit, the A20 levels are substantially high and strongly inhibit NF- κ B activity. On the contrary, at 30 min, A20 mediated feedback activity is weak due to insufficient A20 expression¹⁰. Thus, the 4-hour data provide a more appropriate regime where A20-mediated negative feedback is fully active, which allows us to compare between feedback (WT) and feedback-deficient (A20^{-/-}) conditions clearly in the dual-fidelity space.

We, therefore, use the published dose-response curves and response statistics at 4 hours of TNF stimulation to compute MI and the 2-WD. We note that the empirical single-cell distributions at 4 hours were not reported in the study. We therefore use the dose-response statistics (mean concentrations and standard deviations of NF- κ B and ATF-2) and construct the output distribution at each TNF concentration, $P_{Z|X}(z|x)$, as a Gaussian distribution. See *SI Text* for the mean concentration and standard deviation of single-cell distributions as a function of TNF concentration, extracted from Cheong *et al.*¹⁰. To obtain the input and output marginals, $P_X(x)$ and $P_Z(z)$, we apply an MI-constrained reconstruction strategy, where the input marginal is optimized until the MI calculated from our approximate distributions matches the MI values reported in Cheong *et al.*¹⁰ (see *SI text*). This procedure yields joint and marginal distributions that are consistent with both the published statistics and the reported MI. From these reconstructed marginals, we then compute the 2-WD using the quantile-based definition, which is appropriate here since both input and output distributions are one-dimensional. We note that the TNF concentrations (X) are expressed in ng/mL, while response levels (Z) are measured in arbitrary units (a.u.). We, thus, rescale the response quantiles to the input scale before computing the 2-WD (see *SI Text*).

Acknowledgements

S.I. is supported by JSPS KAKENHI Grants No. 22H01141, No. 23H00467, and No. 24H00834, and UTEC-UTokyo FSI Research Grant Program, and JST ERATO Grant Number JPMJER2302.

Author Contributions

MN and SI designed the research and wrote the paper. MN performed the theoretical analysis and analyzed data.

References

1. Kærn, M., Elston, T. C., Blake, W. J. & Collins, J. J. Stochasticity in gene expression: from theories to phenotypes. *Nat. Rev. Genet.* **6**, 451–464 (2005).
2. Shahrezaei, V. & Swain, P. S. Analytical distributions for stochastic gene expression. *Proc. Natl. Acad. Sci. U. S. A.* **105**, 17256–17261 (2008).
3. Eldar, A. & Elowitz, M. B. Functional roles for noise in genetic circuits. *Nature* **467**, 167–173 (2010).
4. Tsimring, L. S. Noise in biology. *Rep. Prog. Phys.* **77**, 026601 (2014).
5. Shannon, C. E. The mathematical theory of communication. *Bell. Syst. Tech. J.* **27**, 379–423 (1948).
6. Shannon, C. E. & Weaver, W. *The Mathematical Theory of Communication* (University of Illinois Press, Urbana, 1963).
7. Mehta, P., Goyal, S., Long, T., Bassler, B. L. & Wingreen, N. S. Information processing and signal integration in bacterial quorum sensing. *Mol. Syst. Biol.* **5**, 325 (2009).

8. Waltermann, C. & Klipp, E. Information theory based approaches to cellular signaling. *Biochim. Biophys. Acta* **1810**, 924–932 (2011).
9. Uda, S. *et al.* Robustness and compensation of information transmission of signaling pathways. *Science* **341**, 558–561 (2013).
10. Cheong, R., Rhee, A., Wang, C. J., Nemenman, I. & Levchenko, A. Information transduction capacity of noisy biochemical signaling networks. *Science* **334**, 354–358 (2011).
11. Tkačik, G. & Bialek, W. Information processing in living systems. *Annu. Rev. Condens. Matter Phys.* **7**, 89–117 (2016).
12. Tostevin, F. & ten Wolde, P. R. Mutual information between input and output trajectories of biochemical networks. *Phys. Rev. Lett.* **102**, 218101 (2009).
13. Bowsher, C. G. & Swain, P. S. Environmental sensing, information transfer, and cellular decision-making. *Curr. Opin. Biotechnol.* **28**, 149–155 (2014).
14. Gregor, T., Tank, D. W., Wieschaus, E. F. & Bialek, W. Probing the limits to positional information. *Cell* **130**, 153–164 (2007).
15. Lansky, P., Polito, F. & Sacerdote, L. Input-output consistency in integrate and fire interconnected neurons. *Appl. Math. Comput.* **440**, 127630 (2023).
16. Nunns, H. & Goentoro, L. Signaling pathways as linear transmitters. *eLife* **7**, e33617 (2018).
17. Andrews, S. S., Brent, R. & Balázsi, G. Transferring information without distortion. *eLife* **7**, e41894 (2018).
18. Becskei, A., Séraphin, B. & Serrano, L. Positive feedback in eukaryotic gene networks: cell differentiation by graded to binary response conversion. *EMBO J.* **20**, 2528–2535 (2001).
19. Biggar, S. R. & Crabtree, G. R. Cell signaling can direct either binary or graded transcriptional responses. *EMBO J.* **20**, 3167–3176 (2001).
20. Takahashi, S. & Pryciak, P. M. Membrane localization of scaffold proteins promotes graded signaling in the yeast map kinase cascade. *Curr. Biol.* **18**, 1184–1191 (2008).
21. Kramar, M., Hahn, L., Walczak, A. M., Mora, T. & Coppey, M. Single cells can resolve graded stimuli. *PRX Life* **3**, 043016 (2025).
22. Sarkar, S., Ali, M. Z. & Choubey, S. Efficacy of information transmission in cellular communication. *Phys. Rev. Res.* **5**, 013092 (2023).
23. Kussell, E. & Leibler, S. Phenotypic diversity, population growth, and information in fluctuating environments. *Science* **309**, 2075–2078 (2005).
24. Billman, G. E. Homeostasis: The underappreciated and far too often ignored central organizing principle of physiology. *Front. Physiol.* **11**, 200 (2020).
25. Valls, P. O. & Esposito, A. Signalling dynamics, cell decisions, and homeostatic control in health and disease. *Curr. Opin. Cell Biol.* **75**, 102066 (2022).
26. Cover, T. M. & Thomas, J. A. *Elements of Information Theory* (Wiley-Interscience, New York, 1991).
27. Villani, C. *Optimal Transport: Old and New*, vol. 338 (Springer Berlin Heidelberg, 2008).
28. Schiebinger, G. *et al.* Optimal-transport analysis of single-cell gene expression identifies developmental trajectories in reprogramming. *Cell* **176**, 928–943 (2019).
29. Demetci, P., Santorella, R., Sandstede, B., Noble, W. S. & Singh, R. Scot: Single-cell multi-omics alignment with optimal transport. *J. Comp. Biol.* **29**, 3–18 (2022).

30. Cao, K., Gong, Q., Hong, Y. & Wan, L. A unified computational framework for single-cell data integration with optimal transport. *Nat. Commun.* **13**, 1–14 (2022).
31. Kawakita, G., Zeleznikow-Johnston, A., Tsuchiya, N. & Oizumi, M. Gromov–wasserstein unsupervised alignment reveals structural correspondences between the color similarity structures of humans and large language models. *Sci. Rep.* **14**, 15917 (2024).
32. Cuturi, M. Sinkhorn distances: Lightspeed computation of optimal transport. *Adv. neural information processing systems* **26** (2013).
33. Bialek, W. *Biophysics: Searching for principles* (Princeton University Press, Princeton, 2012).
34. Jordan, R., Kinderlehrer, D. & Otto, F. The variational formulation of the Fokker–Planck equation. *SIAM journal on mathematical analysis* **29**, 1–17 (1998).
35. Ito, S. Geometric thermodynamics for the Fokker–Planck equation: stochastic thermodynamic links between information geometry and optimal transport. *Inf. geometry* **7**, 441–483 (2024).
36. Oikawa, S., Nakayama, Y., Ito, S., Sagawa, T. & Toyabe, S. Experimentally achieving minimal dissipation via thermodynamically optimal transport. *Nat. Commun.* **16**, 10424 (2025).
37. Zambrano, S., De Toma, I., Piffer, A., Bianchi, M. E. & Agresti, A. NF- κ B oscillations translate into functionally related patterns of gene expression. *eLife* **5**, e09100 (2016).
38. van Kampen, N. G. *Stochastic Processes in Physics and Chemistry, 3rd ed.* (North-Holland, Amsterdam, 2007).
39. Gardiner, C. W. *Stochastic Methods: A Handbook for the Natural and Social Sciences, 4th ed.* (Springer, Berlin, 2009).
40. Mangan, S. & Alon, U. Structure and function of the feed-forward loop network motif. *Proc. Natl. Acad. Sci. U.S.A.* **100**, 11980–11985 (2003).
41. Alon, U. *An Introduction to Systems Biology: Design Principles of Biological Circuits* (CRC Press, Boca Raton, FL, 2006).
42. Mangan, S., Itzkovitz, S., Zaslaver, A. & Alon, U. The incoherent feed-forward loop accelerates the response-time of the gal system of Escherichia coli. *J. Mol. Biol.* **356**, 1073–1081 (2006).
43. Shen-Orr, S. S., Milo, R., Mangan, S. & Alon, U. Network motifs in the transcriptional regulation network of Escherichia coli. *Nat. Genet.* **31**, 64–68 (2002).
44. Alon, U. Network motifs: theory and experimental approaches. *Nat. Rev. Genet.* **8**, 450–461 (2007).
45. Lahav, G. *et al.* Dynamics of the p53-mdm2 feedback loop in individual cells. *Nat. Genet.* **36**, 147–150 (2004).
46. Barkai, N. & Leibler, S. Robustness in simple biochemical networks. *Nature* **387**, 913–917 (1997).
47. Stelling, J., Sauer, U., Szallasi, Z., Doyle, F. & Doyle, J. Robustness of cellular functions. *Cell* **118**, 675–685 (2004).
48. Gelbrich, M. On a formula for the L^2 Wasserstein metric between measures on Euclidean and Hilbert spaces. *Math. Nachr.* **147**, 185–203 (1990).
49. Nagayama, R., Yoshimura, K., Kolchinsky, A. & Ito, S. Geometric thermodynamics of reaction-diffusion systems: Thermodynamic trade-off relations and optimal transport for pattern formation. *Phys. Rev. Res.* **7**, 033011 (2025).
50. Gardner, T. S., Cantor, C. R. & Collins, J. J. Construction of a genetic toggle switch in Escherichia coli. *Nature* **403**, 339–342 (2000).

51. Elowitz, M. B. & Leibler, S. A synthetic oscillatory network of transcriptional regulators. *Nature* **403**, 335–338 (2000).
52. Elowitz, M. B., Levine, A. J., Siggia, E. D. & Swain, P. S. Stochastic gene expression in a single cell. *Science* **297**, 1183–1186 (2002).
53. Bintu, L. *et al.* Transcriptional regulation by the numbers: models. *Curr. Opin. Genet. Dev.* **15**, 116–124 (2005).
54. Ziv, E., Nemenman, I. & Wiggins, C. H. Optimal signal processing in small stochastic biochemical networks. *PLoS ONE* **2**, e1077 (2007).
55. Tkačik, G., Callan, C. G. & Bialek, W. Information flow and optimization in transcriptional regulation. *Proc. Natl. Acad. Sci. U.S.A.* **105**, 12265–12270 (2008).
56. Tkačik, G., Gregor, T. & Bialek, W. The role of input noise in transcriptional regulation. *PLoS ONE* **3**, e2774 (2008).
57. de Ronde, W. H., Tostevin, F. & Ten Wolde, P. R. Feed-forward loops and diamond motifs lead to tunable transmission of information in the frequency domain. *Phys. Rev. E* **86**, 021913 (2012).
58. Walczak, A. M., Mugler, A. & Wiggins, C. H. Analytic methods for modeling stochastic regulatory networks. *Methods Mol. Biol.* **880**, 273–322 (2012).
59. Elf, J. & Ehrenberg, M. Fast evaluation of fluctuations in biochemical networks with the linear noise approximation. *Genome Res.* **13**, 2475–2484 (2003).
60. Paulsson, J. Summing up the noise in gene networks. *Nature* **427**, 415–418 (2004).
61. Swain, P. S. Efficient attenuation of stochasticity in gene expression through post-transcriptional control. *J. Mol. Biol.* **344**, 965–976 (2004).
62. Tănase-Nicola, S., Warren, P. B. & ten Wolde, P. R. Signal detection, modularity, and the correlation between extrinsic and intrinsic noise in biochemical networks. *Phys. Rev. Lett.* **97**, 068102 (2006).
63. de Ronde, W. H., Tostevin, F. & ten Wolde, P. R. Effect of feedback on the fidelity of information transmission of time-varying signals. *Phys. Rev. E* **82**, 031914 (2010).
64. Nandi, M., Chattopadhyay, S., Bandyopadhyay, S. & Banik, S. K. Channel assisted noise propagation in a two-step cascade. *Chaos: An Interdiscip. J. Nonlinear Sci.* **34**, 083128 (2024).
65. Tostevin, F. & ten Wolde, P. R. Mutual information in time-varying biochemical systems. *Phys. Rev. E* **81**, 061917 (2010).

Supplementary information for “Decoding cell signaling via optimal transport and information theory”

Mintu Nandi and Sosuke Ito

S1 Analytical formulation of steady-state noise

In this study, we employ linear noise approximation (LNA)^{1,2} on the Langevin equation (see Fig. 3h and Eq. (7) in the main text) to derive analytical expressions for the steady-state fluctuations (noise) of the network motifs. We adopt the following notations: $M \in \{Y, Z\}$ as the indices for dynamical variables, $L \in \{X, Y, Z\}$ as the indices for all variables, $n_M \in \{y, z\}$ as the corresponding state space of M in copy numbers unit, and $n_L \in \{x, y, z\}$ as the corresponding state space of L in copy numbers unit.

We treat the input X of the network motifs as a static source of extrinsic noise. This extrinsic noise is modeled by drawing a random variable x from a Gaussian distribution with the mean μ_X and variance σ_X^2 , i.e., $x \sim \mathcal{N}(\mu_X, \sigma_X^2)$. We note that the value of x is fixed in a single cell. However, individual cells can experience different values of x following the said distribution. Such an assumption makes the input X an extrinsically varying random variable to the downstream stochastic components Y and Z in the network motifs.

The dynamics of the downstream nodes Y and Z are modeled using the Langevin equations (see Fig. 3h and Eq. (7) in the main text), given by

$$\frac{dy}{dt} = f_Y(x, z) - g_Y(y) + \sqrt{2}\Gamma_Y\xi_Y(t), \quad (\text{S1})$$

$$\frac{dz}{dt} = f_Z(x, y) - g_Z(z) + \sqrt{2}\Gamma_Z\xi_Z(t), \quad (\text{S2})$$

where, $f_M(\cdot)$ and $g_M(\cdot)$ represent the production and degradation rates, respectively (see Table S1). Here, y and z represent the copy number of the stochastic variables Y and Z , respectively, with steady-state mean μ_M . The noise terms $\xi_Y(t)$ and $\xi_Z(t)$ are independent Gaussian white noise processes with zero mean and unit variance, satisfying $\xi_M(t)\xi_{M'}(t') = \delta_{MM'}\delta(t - t')$, where $M' \in \{Y, Z\}$ ^{1,3-6}. Here, Γ_Y and Γ_Z characterize the strength of the intrinsic stochasticity in the dynamics of Y and Z , respectively.

We note that this framework approximates the underlying master equation by treating the system as a continuous Markov process driven by Gaussian white noise. The usual derivation of the LNA proceeds with the system size expansion of the underlying master equation, which yields the Fokker-Planck equation for the stochastic fluctuations^{1,2}. From this Fokker-Planck equation, one can write the steady-state Lyapunov equation for the covariance matrix, which, upon solving, provides the closed-form expressions of the steady-state variances and covariances in gene regulatory motifs (the derivation is scripted in⁷). In the present study, we adopt a simplified approach by applying the LNA to the Langevin equations [Eqs. (S1) and (S2)] to derive the steady-state variances and covariances of the network components. This simplified method approximates the steady-state statistics well under the assumption that the copy numbers of the stochastic variables are sufficiently large and the fluctuations around the mean are small, as described in earlier studies^{3,8-10}.

To apply the LNA, we define the stochastic fluctuations in Y and Z around their mean by $\delta y = y - \mu_Y$ and $\delta z = z - \mu_Z$, under the assumption that δy and δz are sufficiently small. We note that in the standard LNA formalism, the copy number of each species is decomposed as $n_M = \Omega\phi_M + \Omega^{1/2}\epsilon_M$, where ϕ_M denotes the macroscopic concentration, ϵ_M represents the mesoscopic fluctuation, and Ω refers to the system size. Now defining $\mu_M := \Omega\phi_M$ and $\delta n_M := \Omega^{1/2}\epsilon_M$, we obtain the relative fluctuation scales as $\delta n_M/\mu_M = \mathcal{O}(\Omega^{-1/2})$, which verifies our definition of fluctuations in the limit of large Ω with the standard

LNA formalism^{1,2}. Additionally, we also define the static extrinsic fluctuation of input X by $\delta x = x - \mu_X$, with the assumption that δx is small enough so that linear response in δx remains valid for large μ_X . We note here that δx propagates to the downstream nodes Y and Z through the production rate function $f_M(\cdot)$.

Now, by linearizing the production [$f_M(\cdot)$] and degradation [$g_M(\cdot)$] functions upto first order using Taylor expansion around the steady-states, we obtain,

$$f_Y(x, z) = f_Y(\mu_X + \delta x, \mu_Z + \delta z) = f_Y(\mu_X, \mu_Z) + f'_{YX}(\mu_X, \mu_Z)\delta x + f'_{YZ}(\mu_X, \mu_Z)\delta z \quad (\text{S3})$$

$$f_Z(x, y) = f_Z(\mu_X + \delta x, \mu_Y + \delta y) = f_Z(\mu_X, \mu_Y) + f'_{ZX}(\mu_X, \mu_Y)\delta x + f'_{ZY}(\mu_X, \mu_Y)\delta y \quad (\text{S4})$$

where $f_Y(\mu_X, \mu_Z)$ and $f_Z(\mu_X, \mu_Y)$ denote the production rates of Y and Z at the steady-state. Furthermore, f'_{ML} characterizes the regulatory sensitivities and is defined as the partial derivative of f_M with respect to n_L evaluated in the steady-state, i.e., $f'_{ML} = \partial f_M / \partial n_L$. For the degradation rates, which are first-order reactions (see Table S1), the expansion is exact:

$$g_Y(y) = g_Y(\mu_Y + \delta y) = \tau_Y^{-1}(\mu_Y + \delta y), \quad (\text{S5})$$

$$g_Z(z) = g_Z(\mu_Z + \delta z) = \tau_Z^{-1}(\mu_Z + \delta z), \quad (\text{S6})$$

where, τ_M^{-1} is the degradation rate constant.

The expressions obtained by applying the expected value to both sides of Eqs. (S1) and (S2) can be approximately written as,

$$\frac{d\mu_Y}{dt} = f_Y(\mu_X, \mu_Z) - \tau_Y^{-1}\mu_Y, \quad (\text{S7})$$

$$\frac{d\mu_Z}{dt} = f_Z(\mu_X, \mu_Y) - \tau_Z^{-1}\mu_Z, \quad (\text{S8})$$

where we used the expressions of the first-order Taylor expansions [Eqs. (S3-S6)] and $\overline{\delta x} = \overline{\delta y} = \overline{\delta z} = 0$.

We, now, rewrite Eqs. (S1) and (S2) in terms of the fluctuations δy and δz by using Eqs. (S3-S8), we obtain the linearized equations of the form,

$$\frac{d\delta y}{dt} = f'_{YX}(\mu_X, \mu_Z)\delta x + f'_{YZ}(\mu_X, \mu_Z)\delta z - \tau_Y^{-1}\delta y + \sqrt{2}\Gamma_Y\xi_Y(t), \quad (\text{S9})$$

$$\frac{d\delta z}{dt} = f'_{ZX}(\mu_X, \mu_Y)\delta x + f'_{ZY}(\mu_X, \mu_Y)\delta y - \tau_Z^{-1}\delta z + \sqrt{2}\Gamma_Z\xi_Z(t). \quad (\text{S10})$$

Writing these equations in the matrix form, we obtain,

$$\frac{d\boldsymbol{\delta}}{dt} = (\delta x)\mathbf{a} + \mathbf{J}\boldsymbol{\delta} + \sqrt{2}\boldsymbol{\Gamma}\boldsymbol{\xi}(t), \quad (\text{S11})$$

where,

$$\boldsymbol{\delta} = \begin{pmatrix} \delta y \\ \delta z \end{pmatrix}, \quad \mathbf{a} = \begin{pmatrix} f'_{YX}(\mu_X, \mu_Z) \\ f'_{ZX}(\mu_X, \mu_Y) \end{pmatrix}, \quad \mathbf{J} = \begin{pmatrix} -\tau_Y^{-1} & f'_{YZ}(\mu_X, \mu_Z) \\ f'_{ZY}(\mu_X, \mu_Y) & -\tau_Z^{-1} \end{pmatrix},$$

$$\boldsymbol{\Gamma} = \begin{pmatrix} \Gamma_Y & 0 \\ 0 & \Gamma_Z \end{pmatrix}, \quad \boldsymbol{\xi}(t) = \begin{pmatrix} \xi_Y(t) \\ \xi_Z(t) \end{pmatrix}.$$

Here \mathbf{J} represents the Jacobian evaluated in the steady-state. To ensure the steady-state is stable, we assume $\det(\mathbf{J}) = \tau_Y^{-1}\tau_Z^{-1} - f'_{YZ}(\mu_X, \mu_Z)f'_{ZY}(\mu_X, \mu_Y) > 0$.

We now recast Eq. (S11) as,

$$d\boldsymbol{\delta} = (\delta x)\mathbf{a}dt + \mathbf{J}\boldsymbol{\delta}dt + \sqrt{2}\boldsymbol{\Gamma}d\mathbf{B}, \quad (\text{S12})$$

Table S1. Production and degradation functions for different network motifs. α_M and τ_M^{-1} denote production and degradation rate constants, respectively, and K_{LM} is the dissociation constant of regulator L from the promoter of gene of M . The parameters K_{XY} and K_{ZY} define the BAPs θ_X and θ_Z , respectively. We note that, in general, the production function can be written in the product of the Hill forms $f_M(n_L) = \alpha_M[n_L^h/(K_{LM}^h + n_L^h)]$ for activation and $f_M(n_L) = \alpha_M[(K_{LM}^h/(K_{LM}^h + n_L^h))]$ for repression, where the Hill coefficient h captures the degree of cooperativity. In the present analysis, we use $h = 1$ to ensure that the steady-state probability distributions of the components in feedback loops remain monostable.

Function	SC, C1-FFL, I1-FFL	PFL	DNFL, NFL	
$f_Y(x, z)$	$\alpha_Y \frac{x}{K_{XY} + x}$	$\alpha_Y \left[\frac{x}{K_{XY} + x} + \frac{z}{K_{ZY} + z} \right]$	$\alpha_Y \left[\frac{x}{K_{XY} + x} + \frac{K_{ZY}}{K_{ZY} + z} \right]$	
$f_Y(\mu_X, \mu_Z)$	$\alpha_Y \frac{\mu_X}{K_{XY} + \mu_X}$	$\alpha_Y \left[\frac{\mu_X}{K_{XY} + \mu_X} + \frac{\mu_Z}{K_{ZY} + \mu_Z} \right]$	$\alpha_Y \left[\frac{\mu_X}{K_{XY} + \mu_X} + \frac{K_{ZY}}{K_{ZY} + \mu_Z} \right]$	
$f'_{YX}(\mu_X, \mu_Z)$	$\alpha_Y \frac{K_{XY}}{(K_{XY} + \mu_X)^2}$	$\alpha_Y \frac{K_{XY}}{(K_{XY} + \mu_X)^2}$	$\alpha_Y \frac{K_{XY}}{(K_{XY} + \mu_X)^2}$	
$f'_{YZ}(\mu_X, \mu_Z)$	0	$\alpha_Y \frac{K_{ZY}}{(K_{ZY} + \mu_Z)^2}$	$-\alpha_Y \frac{K_{ZY}}{(K_{ZY} + \mu_Z)^2}$	
Function	SC, PFL, NFL	DNFL	C1-FFL	I1-FFL
$f_Z(x, y)$	$\alpha_Z \frac{y}{K_{YZ} + y}$	$\alpha_Z \frac{K_{YZ}}{K_{YZ} + y}$	$\alpha_Z \frac{x}{K_{XZ} + x} \cdot \frac{y}{K_{YZ} + y}$	$\alpha_Z \frac{x}{K_{XZ} + x} \cdot \frac{K_{YZ}}{K_{YZ} + y}$
$f_Z(\mu_X, \mu_Y)$	$\alpha_Z \frac{\mu_Y}{K_{YZ} + \mu_Y}$	$\alpha_Z \frac{K_{YZ}}{K_{YZ} + \mu_Y}$	$\alpha_Z \frac{\mu_X}{K_{XZ} + \mu_X} \cdot \frac{\mu_Y}{K_{YZ} + \mu_Y}$	$\alpha_Z \frac{\mu_X}{K_{XZ} + \mu_X} \cdot \frac{K_{YZ}}{K_{YZ} + \mu_Y}$
$f'_{ZX}(\mu_X, \mu_Y)$	0	0	$\alpha_Z \frac{K_{XZ}}{(K_{XZ} + \mu_X)^2} \cdot \frac{\mu_Y}{K_{YZ} + \mu_Y}$	$\alpha_Z \frac{K_{XZ}}{(K_{XZ} + \mu_X)^2} \cdot \frac{K_{YZ}}{K_{YZ} + \mu_Y}$
$f'_{ZY}(\mu_X, \mu_Y)$	$\alpha_Z \frac{K_{YZ}}{(K_{YZ} + \mu_Y)^2}$	$-\alpha_Z \frac{K_{YZ}}{(K_{YZ} + \mu_Y)^2}$	$\alpha_Z \frac{\mu_X}{K_{XZ} + \mu_X} \cdot \frac{K_{YZ}}{(K_{YZ} + \mu_Y)^2}$	$-\alpha_Z \frac{\mu_X}{K_{XZ} + \mu_X} \cdot \frac{K_{YZ}}{(K_{YZ} + \mu_Y)^2}$
Degradation functions (all motifs): $g_Y(y) = \tau_Y^{-1}y$, $g_Y(\mu_Y) = \tau_Y^{-1}\mu_Y$; $g_Z(z) = \tau_Z^{-1}z$, $g_Z(\mu_Z) = \tau_Z^{-1}\mu_Z$				

where $d\mathbf{B}$ is the Wiener process^{11,12} that satisfies $\overline{d\mathbf{B}} = \mathbf{0}$ and $\overline{d\mathbf{B}(d\mathbf{B})^\top} = \mathbf{I}dt$. Here, $\mathbf{0}$ is the zero vector, and \mathbf{I} is the identity matrix. Now assuming δ to be the Ito processes, the Ito rule gives $d(\delta\delta^\top) = (d\delta)\delta^\top + \delta(d\delta)^\top + (d\delta)(d\delta)^\top + O(dt^{3/2}) = (d\delta)\delta^\top + \delta(d\delta)^\top + 2(\mathbf{\Gamma}d\mathbf{B})(\mathbf{\Gamma}d\mathbf{B})^\top + O(dt^{3/2})$, where \top stands for the transpose of a matrix and $O(dt^{3/2})$ is Landau's O notation, which ignores orders greater than or equal to $dt^{3/2}$. Using Eq. (S12) on this expansion followed by ensemble averaging yields,

$$\frac{d\overline{\delta\delta^\top}}{dt} = \mathbf{a}\sigma^\top + \sigma\mathbf{a}^\top + \mathbf{J}\Sigma + \Sigma\mathbf{J}^\top + 2\mathbf{D}, \quad (\text{S13})$$

where

$$\sigma := \overline{(\delta x)\delta} = \begin{pmatrix} \sigma_{XY} \\ \sigma_{XZ} \end{pmatrix},$$

represents a covariance vector which contains the covariances between Y and X and between Z and X ,

$$\Sigma := \overline{\delta\delta^\top} = \begin{pmatrix} \sigma_Y^2 & \sigma_{YZ} \\ \sigma_{YZ} & \sigma_Z^2 \end{pmatrix},$$

is the covariance matrix of Y and Z , and $\mathbf{D} := \mathbf{\Gamma}\mathbf{\Gamma}^\top$ denotes the diffusion matrix that also appears in the corresponding Fokker-Planck description.

We here calculate the variance-covariance matrix Σ and the covariance vector σ in the steady-state. Due to the LNA, $\mathbf{D} = \text{diag}(D_Y, D_Z)$ at the steady-state is given by $D_Y = [f_Y(\mu_X, \mu_Z) + g_Y(\mu_Y)]/2$ and

$D_Z = [f_Z(\mu_X, \mu_Y) + g_Z(\mu_Z)]/2$ ¹³. Therefore, we obtain

$$\mathbf{D} = \frac{1}{2} \begin{pmatrix} 2\tau_Y^{-1}\mu_Y & 0 \\ 0 & 2\tau_Z^{-1}\mu_Z \end{pmatrix},$$

where we used $f_Y(\mu_X, \mu_Z) = g_Y(\mu_Y) = \tau_Y^{-1}\mu_Y$ and $f_Z(\mu_X, \mu_Y) = g_Z(\mu_Z) = \tau_Z^{-1}\mu_Z$ because $d\mu_Y/dt = d\mu_Z/dt = 0$ in the steady-state. In the steady-state, $\frac{d\overline{\delta\delta}^\top}{dt} = 0$ also gives,

$$\mathbf{a}\boldsymbol{\sigma}^\top + \boldsymbol{\sigma}\mathbf{a}^\top + \mathbf{J}\boldsymbol{\Sigma} + \boldsymbol{\Sigma}\mathbf{J}^\top + 2\mathbf{D} = 0. \quad (\text{S14})$$

Solving Eq. (S14) for the covariance matrix $\boldsymbol{\Sigma}$ yields,

$$\begin{aligned} \sigma_Y^2 &= \mu_Y + \frac{\tau_Z^{-1}f'_{YZ}(\mu_Y f'_{ZY} + \mu_Z f'_{YZ})}{(\tau_Y^{-1} + \tau_Z^{-1})(\tau_Y^{-1}\tau_Z^{-1} - f'_{YZ}f'_{ZY})} + \frac{f'_{YZ}(\tau_Z^{-1}f'_{ZX} - f'_{YX}f'_{ZY}) + \tau_Z^{-1}f'_{YX}(\tau_Y^{-1} + \tau_Z^{-1})}{(\tau_Y^{-1} + \tau_Z^{-1})(\tau_Y^{-1}\tau_Z^{-1} - f'_{YZ}f'_{ZY})}\sigma_{XY} \\ &\quad + \frac{f'_{YZ}(f'_{YZ}f'_{ZX} + \tau_Z^{-1}f'_{YX})}{(\tau_Y^{-1} + \tau_Z^{-1})(\tau_Y^{-1}\tau_Z^{-1} - f'_{YZ}f'_{ZY})}\sigma_{XZ}, \end{aligned} \quad (\text{S15})$$

$$\begin{aligned} \sigma_Z^2 &= \mu_Z + \frac{\tau_Y^{-1}f'_{ZY}(\mu_Y f'_{ZY} + \mu_Z f'_{YZ})}{(\tau_Y^{-1} + \tau_Z^{-1})(\tau_Y^{-1}\tau_Z^{-1} - f'_{YZ}f'_{ZY})} + \frac{f'_{ZY}(f'_{YX}f'_{ZY} + \tau_Y^{-1}f'_{ZX})}{(\tau_Y^{-1} + \tau_Z^{-1})(\tau_Y^{-1}\tau_Z^{-1} - f'_{YZ}f'_{ZY})}\sigma_{XY} \\ &\quad + \frac{f'_{ZY}(\tau_Y^{-1}f'_{YX} - f'_{YZ}f'_{ZX}) + \tau_Y^{-1}f'_{ZX}(\tau_Y^{-1} + \tau_Z^{-1})}{(\tau_Y^{-1} + \tau_Z^{-1})(\tau_Y^{-1}\tau_Z^{-1} - f'_{YZ}f'_{ZY})}\sigma_{XZ}, \end{aligned} \quad (\text{S16})$$

$$\begin{aligned} \sigma_{YZ} &= \frac{\tau_Y^{-1}\tau_Z^{-1}(\mu_Y f'_{ZY} + \mu_Z f'_{YZ})}{(\tau_Y^{-1} + \tau_Z^{-1})(\tau_Y^{-1}\tau_Z^{-1} - f'_{YZ}f'_{ZY})} + \frac{\tau_Z^{-1}(f'_{YX}f'_{ZY} + \tau_Y^{-1}f'_{ZX})}{(\tau_Y^{-1} + \tau_Z^{-1})(\tau_Y^{-1}\tau_Z^{-1} - f'_{YZ}f'_{ZY})}\sigma_{XY} \\ &\quad + \frac{\tau_Y^{-1}(f'_{YZ}f'_{ZX} + \tau_Z^{-1}f'_{YX})}{(\tau_Y^{-1} + \tau_Z^{-1})(\tau_Y^{-1}\tau_Z^{-1} - f'_{YZ}f'_{ZY})}\sigma_{XZ}. \end{aligned} \quad (\text{S17})$$

Here, we have used the following short-hand notations: $f'_{YX}(\mu_X, \mu_Z) =: f'_{YX}$, $f'_{YZ}(\mu_X, \mu_Z) =: f'_{YZ}$, $f'_{ZX}(\mu_X, \mu_Y) =: f'_{ZX}$, and $f'_{ZY}(\mu_X, \mu_Y) =: f'_{ZY}$. These expressions are obtained as functions of regulatory sensitivities (f'_{ML}), some biochemical parameters, and the elements of $\boldsymbol{\sigma}$. To derive $\boldsymbol{\sigma}$ in the steady-state, we multiply Eq. (S12) by δx followed by ensemble averaging in the steady-state, which yields,

$$\frac{d\boldsymbol{\sigma}}{dt} = (\delta x)\frac{d\overline{\delta\delta}}{dt} = \mathbf{a}\sigma_X^2 + \mathbf{J}\boldsymbol{\sigma} = 0, \quad (\text{S18})$$

where $\sigma_X^2 = \overline{\delta x^2}$. In Eq. (S18), we use $\overline{(\delta x)\sqrt{2\mathbf{\Gamma}\boldsymbol{\xi}}} = 0$ due to uncorrelation. Solving this equation yields the exact expressions of the elements of $\boldsymbol{\sigma}$ in terms of the input variance σ_X^2 , as follows,

$$\sigma_{XY} = \frac{f'_{YZ}f'_{ZX} + \tau_Z^{-1}f'_{YX}}{\tau_Y^{-1}\tau_Z^{-1} - f'_{YZ}f'_{ZY}}\sigma_X^2, \quad (\text{S19})$$

$$\sigma_{XZ} = \frac{f'_{YX}f'_{ZY} + \tau_Y^{-1}f'_{ZX}}{\tau_Y^{-1}\tau_Z^{-1} - f'_{YZ}f'_{ZY}}\sigma_X^2. \quad (\text{S20})$$

By substituting Eqs. (S19) and (S20) into the expression for the output variance σ_Z^2 , we obtain a closed-form expression of σ_Z^2 in terms of the input variance,

$$\sigma_Z^2 = \mu_Z + \phi_1 + \phi_2\sigma_X^2, \quad (\text{S21})$$

where,

$$\begin{aligned}\phi_1 &= \frac{\tau_Y^{-1} f'_{ZY} (\mu_Y f'_{ZY} + \mu_Z f'_{YZ})}{(\tau_Y^{-1} + \tau_Z^{-1}) (\tau_Y^{-1} \tau_Z^{-1} - f'_{YZ} f'_{ZY})}, \\ \phi_2 &= \frac{(f'_{YX} f'_{ZY} + \tau_Y^{-1} f'_{ZX})^2}{(\tau_Y^{-1} \tau_Z^{-1} - f'_{YZ} f'_{ZY})^2}.\end{aligned}$$

We quantify the output noise of Z using the squared coefficient of variation, $\eta_Z^2 = \sigma_Z^2/\mu_Z^2$. Using Eq. (S21), we can write the closed-form expression of η_Z^2 as,

$$\eta_Z^2 = \frac{1}{\mu_Z} + \Phi_1 + \Phi_2 \eta_X^2, \quad (\text{S22})$$

where, $\eta_X^2 = \sigma_X^2/\mu_X^2$ characterizes the noise in the input, and the coefficients $\Phi_1 = \phi_1/\mu_Z^2$ and $\Phi_2 = \mu_X^2 \phi_2/\mu_Z^2$ collect the contributions from the intermediate terms. The normalized covariance between X and Z is defined as $\zeta_{XZ} = \sigma_{XZ}/(\mu_X \mu_Z)$ and its closed-form expression can be written from Eq. (S20) as,

$$\zeta_{XZ} = \Psi \eta_X^2, \quad (\text{S23})$$

where,

$$\Psi = \frac{\mu_X (f'_{YX} f'_{ZY} + \tau_Y^{-1} f'_{ZX})}{\mu_Z (\tau_Y^{-1} \tau_Z^{-1} - f'_{YZ} f'_{ZY})}.$$

The noise of Y , $\eta_Y^2 = \sigma_Y^2/\mu_Y^2$, can similarly be defined from Eq. (S15). η_Z^2 and ζ_{XZ} are used to calculate the mutual information (MI) and the 2-Wasserstein distance (2-WD) using Eqs. (8) and (10) given in the main text.

S2 Binding affinities

The output noise and the input–output normalized covariance depend on several biochemical parameters, including mean expression levels (μ_L), the degradation rate constants (τ_M^{-1}), and the regulatory sensitivities (f'_{ML}). We refer to f'_{ML} as regulatory sensitivities since they capture the slope of the input-output regulatory functions in the steady-state, quantifying how strongly a small change in the regulator L influences the expression of the gene M . These sensitivity terms themselves are functions of the production rate constants (α_M) and the dissociation constants (K_{LM}) (see Table S1). The dissociation constant K_{LM} is a coarse-grained parameter that characterizes the binding affinity of transcription factor (TF) L to the promoter of the gene of M . A smaller K_{LM} corresponds to a reduced dissociation rate, reflecting a higher affinity. In this study, we systematically vary the promoter properties of the gene of Y (the intermediate node common to all motifs) to examine how binding affinity influences both informational and geometric fidelities.

In the simple cascade (SC), coherent type-1 feed-forward loop (C1-FFL), and incoherent type-1 feed-forward loop (I1-FFL), the promoter of Y interacts with X , characterized by the parameter K_{XY} . In the positive feedback loop (PFL), double negative feedback loop (DNFL), and negative feedback loop (NFL), the promoter of Y interacts with both X and Z , governed by K_{XY} and K_{ZY} . We tune these parameters around the half-maximal regulation ($K_{LM} = \mu_L$)¹⁴. To quantify deviations from this reference, we define binding affinity parameters (BAPs) as $\theta_X = K_{XY}/\mu_X$ and $\theta_Z = K_{ZY}/\mu_Z$. By construction, $\theta_X = 1$ and $\theta_Z = 1$ corresponds to half-maximal regulation of Y 's promoter by X and Z . If $\theta_X < 1$ and $\theta_Z < 1$, this indicates strong binding affinities of X and Z to the Y 's promoter, and if $\theta_X > 1$ and $\theta_Z > 1$, this represents weak binding affinities (see Fig. 4 in the main text).

The introduction of BAP as a measure of promoter affinity serves two key purposes. First, it separates

binding affinity from absolute expression levels, so that comparisons across different motifs do not depend on the scale of protein copy numbers. Second, it directly links BAP to the regulatory input–output curve, where K sets the half-saturation point. Functionally, promoters with strong affinities can drive rapid and decisive state changes, while weak affinities give rise to graded responses and dampened variability. Such variations can be engineered through targeted promoter mutations or the synthetic modification of TF–DNA binding sites, making it an experimentally tunable parameter.

S3 Model Parameters

To optimize the objective function \mathcal{L} with respect to the input noise η_X^2 (Eq. (6) in the main text), we fixed the mean copy number of all three proteins to $\mu_X = \mu_Y = \mu_Z = 100$. This ensures that copy number driven noise remains consistent across species, allowing us to isolate the role of noise propagation from input to output in shaping the dual-fidelity landscape of different network motifs. Choosing copy numbers on the order of a hundred also justifies the use of Gaussian approximations^{5,15}.

The degradation rates are chosen as $\tau_Y^{-1} = 1.0$ and $\tau_Z^{-1} = 10.0$ to enforce a separation of timescales in which Y decays slowly and Z decays rapidly. Such a hierarchy is a common requirement for reliable signaling: a slower upstream component (Y) preserves memory of prior input (X), while a faster downstream component (Z) can rapidly track changes without accumulating excessive noise. This arrangement facilitates efficient information transmission along the motif⁷. Within this regime, we analyze how input noise can be tuned to optimize the trade-off between informational and geometric fidelity. We next vary each of θ_X and θ_Z across three regimes: < 1 , $= 1$, and > 1 represented by the values 0.5, 1, and 2, respectively. We have nine possible sets of (θ_X, θ_Z) for PFL, DNFL, and NFL motifs. However, for SC, C1-FFL, and I1-FFL, we have three possible values of θ_X only. This allows us to explore how promoter affinities of Y shape the balance between the two fidelities.

For each species, the production rate constants α_M , encapsulated in f_M (see Table S1), are obtained by considering Eqs. (S7) and (S8) in the steady-state. Finally, to map the optimal dual-fidelity profiles, we vary the trade-off parameter λ over the range 10^{-4} to 1. When λ is very small, the optimization is dominated by MI, and as it increases up to unity, the 2-WD progressively balances MI. We choose this range because the numerical scale of MI is much smaller than that of the 2-WD (see Fig. 5 in the main text). Restricting λ to 10^{-4} –1 ensures that both measures enter the optimization on a comparable footing despite their inherent difference in magnitude.

S4 Interpreting 2-Wasserstein distance

The numerical value of the 2-WD is expressed in the same units as the variables being compared. In our theoretical analysis, where system components X and Z are expressed in molecular copy numbers, the 2-WD carries units of molecule count. In contrast, experimental estimates express the 2-WD in units of TNF concentration. The interpretation of $W(X, Z) = 1$ is therefore unit-dependent, yet its conceptual meaning remains consistent: it quantifies the minimal average mismatch between the input and output distributions under an optimal transport plan.

A value of $W(X, Z) = 1$ indicates that, under the optimal mapping between the input and output, the root-mean-square discrepancy between them is one unit. In the copy numbers unit, this corresponds to an average distortion of one molecule per cell between input and output distributions. In the TNF concentration unit, it implies that the signaling pathway cannot reduce the average concentration distortion below one concentration unit, given the observed variability.

Under Gaussian approximation (see Eq. (9) in the main text), $W(X, Z) = 1$ occurs when $(\mu_X - \mu_Z)^2 + (\sigma_X - \sigma_Z)^2 = 1$. This indicates three representative cases: (1) a pure mean shift of one unit ($\mu_Z = \mu_X \pm 1$) with equal standard deviations ($\sigma_Z = \sigma_X$), (2) a pure spread difference of one unit ($\sigma_Z = \sigma_X \pm 1$) with

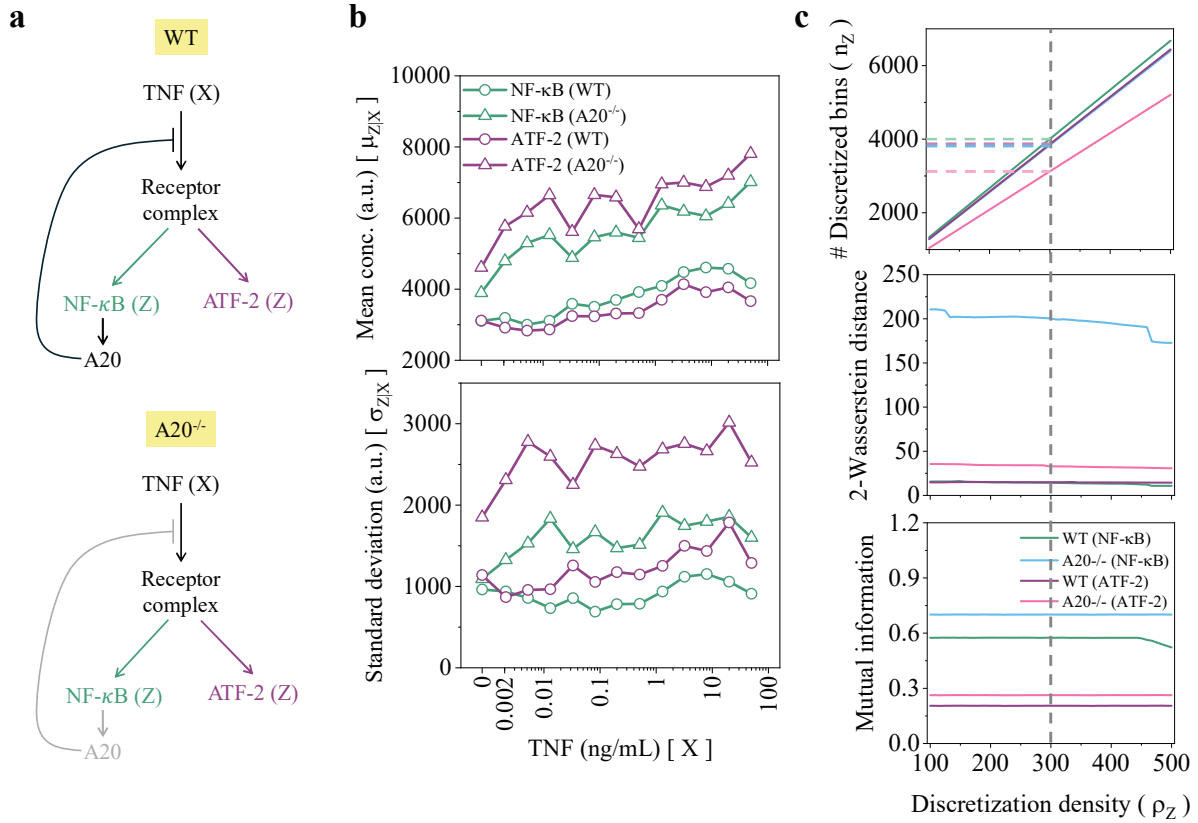


Figure S1. Experimental system. **a** Schematics of TNF signaling in WT and A20^{-/-} cells. **b** The dose-response statistics. **c** Convergence of MI and the 2-WD as a function of discretization.

equal means, or (3) any combination of mean and spread differences satisfying the same relation. This clarifies the biological implications that a nonzero mean shift indicates a systematic bias in the response, while a spread difference reflects the amplification or filtering of input variability. The value $W(X, Z) = 1$ thus serves as a unified measure of the total geometric distortion introduced by the signaling process, whether expressed in theoretical or experimental units.

In the theoretical analysis, we set geometric fidelity $W(X, Z)^{-1} \geq 1$ as the minimum for reliable distributional correspondence (see main text). This threshold corresponds to $W(X, Z) \leq 1$. Under the Gaussian form with equal means (see Sec. S3), the 2-WD reduces to the absolute difference between the input and output standard deviations, so the criterion is simply $|\sigma_X - \sigma_Z| \leq 1$ in the copy number unit. This allows at most a one-molecule difference in spread between the input and output. We choose this threshold because it represents a fundamental unit of discreteness in stochastic gene expression. A standard deviation distortion larger than a single molecule implies the regulatory mechanism is actively reshaping the noise profile beyond the minimal discreteness noise inherent to molecular counting. We note that the numerical value of this threshold is unit-dependent and is strictly meaningful within our theoretical framework, where the 2-WD is measured in copy numbers unit. In experimental settings, where variables are expressed in physical units such as ng/mL or arbitrary fluorescence units, an equivalent threshold must be defined relative to the effective resolution and fluctuation level of the measurement system, rather than by the absolute numerical value alone.

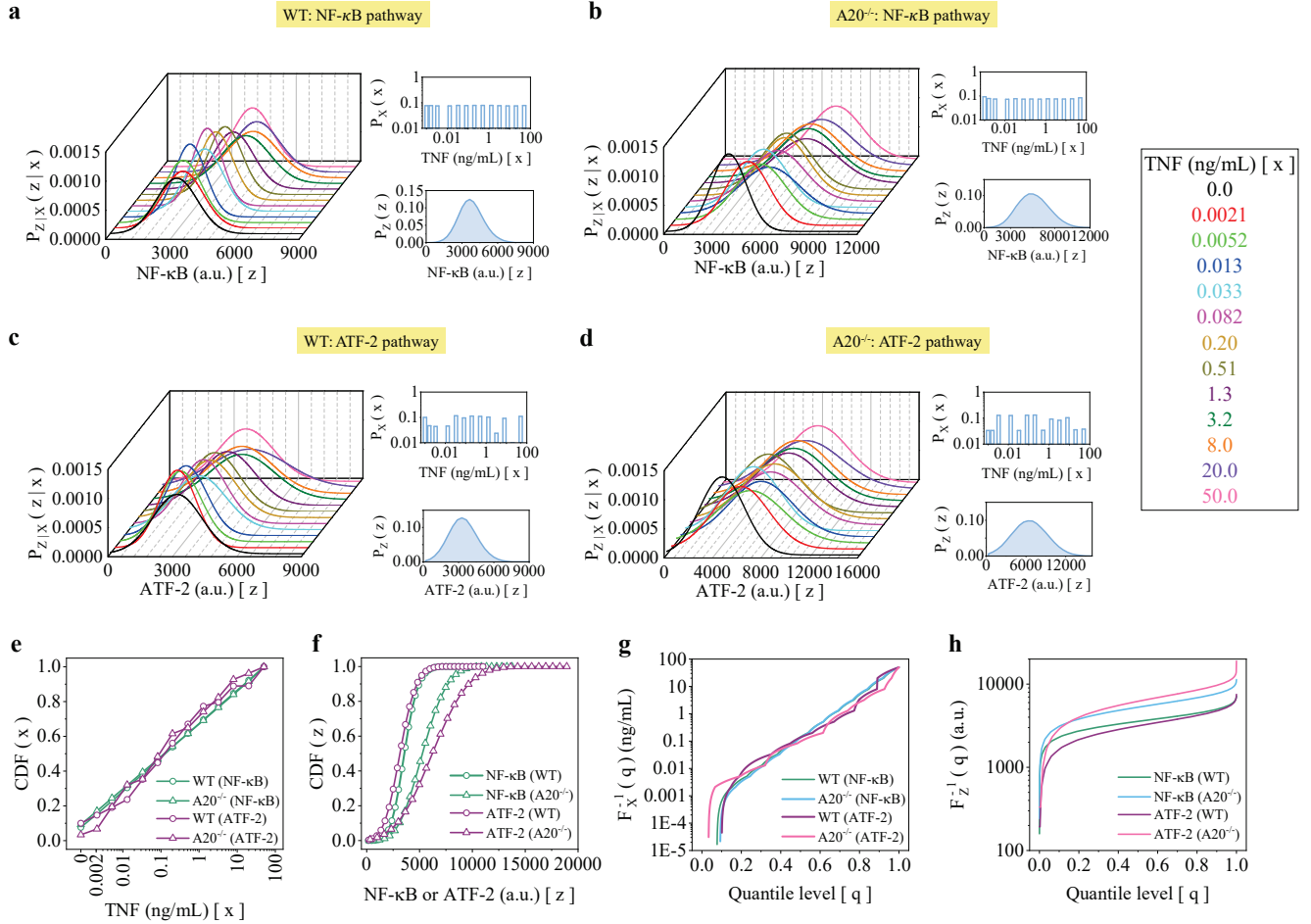


Figure S2. Reconstructed distributions. Gaussian conditionals, optimized input distributions, and output marginals for **a** NF- κ B in WT cells, **b** NF- κ B in A20^{-/-} cells, **c** ATF-2 in WT cells, and **d** ATF-2 in A20^{-/-} cells. **e** CDF of input distribution. **f** CDF output distribution. **g** Quantile function of input distribution. **h** Quantile function of output distribution.

S5 Experimental data analysis

We adopt the single-cell measurements of the NF- κ B and ATF-2 signaling pathways stimulated by TNF (Fig. S1a), reported in Cheong *et al.*¹⁶. We have extracted the reported dose-response statistics for WT and A20^{-/-} cells after 4 hours of TNF stimulation, and we reproduce them in Fig. S1b. In this dataset, we consider the TNF concentration as the input X and either NF- κ B or ATF-2 as the output Z , depending on the pathway analyzed. For each TNF concentration, denoted x_i (ng/mL), the dataset provides the corresponding conditional mean concentration $\mu_{Z|X}(x_i)$ (a.u.), and conditional standard deviation (SD) $\sigma_{Z|X}(x_i)$ (a.u.) for the outputs in both cell types (see Fig. S1b). We note that these statistics are used to generate Fig. 6d in the main text. For numerical evaluation, at each input concentration x_i , we approximate the conditional distributions of NF- κ B and ATF-2 by a Gaussian distribution, defined as,

$$P(z|x_i) = \mathcal{N}\left(\mu_{Z|X}(x_i), \sigma_{Z|X}^2(x_i)\right). \quad (\text{S24})$$

The distributions are discretized on a grid bounded by $z \in [z_{\min}, z_{\max}]$, where,

$$\begin{aligned} z_{\min} &= \max \left(0, \min_i [\mu_{Z|X}(x_i) - 4\sigma_{Z|X}(x_i)] \right), \\ z_{\max} &= \max_i [\mu_{Z|X}(x_i) + 4\sigma_{Z|X}(x_i)], \end{aligned}$$

with normalization $\sum_k P(z_k|x_i)\Delta z = 1$. This choice of discretization is used to ensure consistency, where a single common range for the output variable z could be applied to all input concentrations. Moreover, the bounds are set using $\pm 4\sigma_{Z|X}(x_i)$ because, for approximately Gaussian distributions, we assume that the probability mass outside this range is negligible. This ensures that nearly all biologically relevant variation is retained without allocating computational effort to regions where the density is effectively zero. Now, the grid resolution (number of discretized bins) is chosen adaptively according to,

$$n_Z = \left\lceil \frac{\rho_Z(z_{\max} - z_{\min})}{\min_i [\sigma_{Z|X}(x_i)]} \right\rceil,$$

where, ρ_Z is a tunable discretization density parameter. Scaling ρ_Z with the global output range and the minimum conditional SD ensures that even the narrowest distributions are sampled with sufficient resolution. The ceiling function $\lceil \cdot \rceil$ rounds up the real value to the nearest integer. The stability of this discretization is verified by systematically varying ρ_Z and recalculating all quantities of interest. We find that at $\rho_Z = 300$, both MI and the 2-WD maintain a stable plateau (Fig. S1c), which confirms numerical robustness.

Given a candidate input distribution $P_X(x) = \{P_X(x_i)\}$, the output marginal distribution is given by $P_Z(z) = \sum_i P_X(x_i)P(z|x_i)$ and the discrete form of MI with bin width $\Delta z = (z_{\max} - z_{\min})/n_Z$ gives,

$$I(X; Z) = \sum_{i,k} P_X(x_i)P(z_k|x_i) \log_2 \left[\frac{P(z_k|x_i)}{P_Z(z_k)} \right] \Delta z. \quad (\text{S25})$$

We determine $P_X(x)$ by minimizing $[I(X; Z) - I_{\text{target}}(X; Z)]^2$ subject to $\sum_i P_X(x_i) = 1$ and $0 \leq P_X(x_i) \leq 1$, where $I_{\text{target}}(X; Z)$ denotes the reported values of MI in Cheong *et al.*¹⁶. After optimization, our estimated $I(X; Z)$ matches the reported channel capacity $I_{\text{target}}(X; Z)$ within numerical tolerance. The resulting $P_X(x)$ and $P_Z(z)$ are then used to estimate the 2-WD. The Gaussian approximated $P(z|x)$, the optimal $P_X(x)$ and $P_Z(z)$ are given in Figs. S2a-d for different signaling pathways and experimental conditions.

Since both the input and the output are one-dimensional, we use the quantile-based definition of the 2-WD, which is given by¹⁷,

$$W(X, Z) = \sqrt{\int_0^1 (F_X^{-1}(q) - F_Z^{-1}(q))^2 dq}, \quad (\text{S26})$$

where $F_X^{-1}(q)$ and $F_Z^{-1}(q)$ are the quantile functions of $P_X(x)$ and $P_Z(z)$. Numerically, quantiles are computed from the cumulative distribution functions (CDFs) of $P_X(x)$ and $P_Z(z)$ over 1000 quantile points. The CDFs and quantiles are shown in Figs. S2e-h.

Because the input quantiles are in ng/mL while the output quantiles are in a.u., the two must be expressed on the same scale before evaluating the 2-WD using Eq. (S26). This is necessary because the 2-WD depends explicitly on distances measured in the units of the underlying variable. Our goal here is not to biochemically calibrate fluorescence units, but to ensure that small changes in input and output are compared consistently in the dose range where the response is most sensitive. We therefore define a mapping that aligns output fluctuations with input fluctuations around the point of maximal sensitivity of the dose-response curve. To compute the mapping factor, we fit the experimentally reported discrete

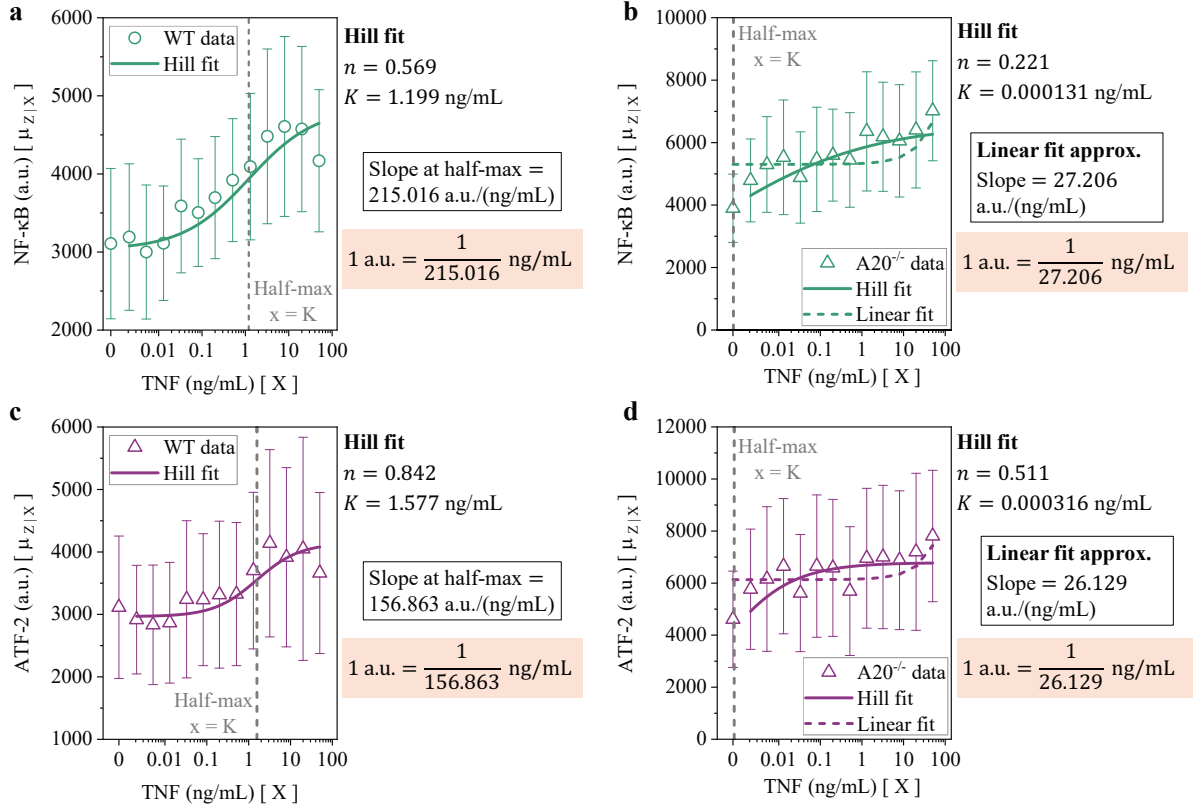


Figure S3. Dose-response fitting and mapping factors. **a** WT cells with Hill fits and slopes at half-maximum for NF- κ B. **b** A20^{-/-} cells with linear fits due to the lack of a sigmoidal profile for NF- κ B. **c** WT cells with Hill fits and slopes at half-maximum for ATF-2. **d** A20^{-/-} cells with linear fits due to the lack of a sigmoidal profile for ATF-2. Slopes define the mapping from a.u. to ng/mL (orange colored block). The mean and corresponding error bars are obtained from the mean and standard deviation, respectively, given in Fig. S1b.

dose-response data $\{\mu_{Z|X}(x_i)\}$ using a continuous Hill function of the form,

$$R(x) = R_{\min} + \frac{R_{\max} - R_{\min}}{1 + (K/x)^n}, \quad (\text{S27})$$

where, x is treated as a continuous approximation of the discrete TNF concentrations x_i . The fitted function satisfies $R(x_i) \approx \mu_{Z|X}(x_i)$ for all measured points. In this expression, R_{\max} and R_{\min} represent the basal and saturating output concentrations, K is the half-maximal TNF concentration, and n is the Hill coefficient. To obtain a consistent mapping factor, we compute the slope of the fitted curve at the half-maximum point, i.e., $x = K$,

$$\left. \frac{dR(x)}{dx} \right|_{x=K} = \frac{n(R_{\max} - R_{\min})}{4K},$$

This slope provides a standardized local gain of the dose-response curve at half-maximum. The half-maximum point corresponds to the region of highest sensitivity and minimal saturation, which contributes most strongly to both mutual information and geometric comparisons in sigmoidal signaling responses. The reciprocal of this slope, with units of ng/mL per a.u., is therefore used as the mapping factor to convert output quantiles into the same units as the input. Anchoring the conversion to this sensitive region avoids distortions arising from shallow, low-dose responses or saturated, high-dose regimes.

We find that the dose-response curve of WT cells is well described by a Hill function with an identifiable

half-maximal concentration K (Figs. S3a,c). In contrast, the dose-response curve of A20^{-/-} does not display a clear sigmoidal regime over the measured dose range, leading to poorly constrained Hill fits and spuriously small estimates of K (Figs. S3b,d). This is consistent with loss of A20-dependent negative feedback, which can reshape the effective input–output relationship (e.g., shift the operating range and reduce the apparent saturation within the probed doses). To obtain a robust scale conversion in this case, we instead use a linear approximation $R(x) = a + bx$ and take the slope b as the mapping factor (Figs. S3b,d). After mapping the output quantiles onto the same scale as the input, we measure the 2-WD for NF- κ B and ATF-2 in both cell types. The error bars in both MI and the 2-WD are estimated using bootstrap resampling.

We note that alternative strategies exist to place input and output distributions on a common scale before computing the 2-WD, such as rescaling each marginal by its standard deviation or by an empirical dynamic range. However, these normalizations can be dominated by low-gain regions of the dose–response, including low-dose noise and high-dose saturation, where changes in input produce little change in output. This issue is particularly relevant for A20^{-/-} cells, which do not exhibit apparent sigmoidal behavior of the dose-response curves over the probed concentration range (Figs. S3b,d). Our slope-based mapping, therefore, defines a common, gain-based scale for comparing geometric fidelity across conditions.

References

1. van Kampen, N. G. *Stochastic Processes in Physics and Chemistry*, 3rd ed. (North-Holland, Amsterdam, 2007).
2. Gardiner, C. W. *Stochastic Methods: A Handbook for the Natural and Social Sciences*, 4th ed. (Springer, Berlin, 2009).
3. Elf, J. & Ehrenberg, M. Fast evaluation of fluctuations in biochemical networks with the linear noise approximation. *Genome Res.* **13**, 2475–2484 (2003).
4. Paulsson, J. Summing up the noise in gene networks. *Nature* **427**, 415–418 (2004).
5. Tănase-Nicola, S., Warren, P. B. & ten Wolde, P. R. Signal detection, modularity, and the correlation between extrinsic and intrinsic noise in biochemical networks. *Phys. Rev. Lett.* **97**, 068102 (2006).
6. de Ronde, W. H., Tostevin, F. & ten Wolde, P. R. Effect of feedback on the fidelity of information transmission of time-varying signals. *Phys. Rev. E* **82**, 031914 (2010).
7. Nandi, M., Chattopadhyay, S., Bandyopadhyay, S. & Banik, S. K. Channel assisted noise propagation in a two-step cascade. *Chaos: An Interdiscip. J. Nonlinear Sci.* **34**, 083128 (2024).
8. Wallace, E. W. J. A simplified derivation of the linear noise approximation. *arXiv* (2010). [arXiv:1004.4280](https://arxiv.org/abs/1004.4280).
9. Wallace, E. W. J., Gillespie, D. T., Sanft, K. R. & Petzold, L. R. Linear noise approximation is valid over limited times for any chemical system that is sufficiently large. *IET Syst. Biol.* **6**, 102–115 (2012).
10. Mugler, A., Tostevin, F. & ten Wolde, P. R. Spatial partitioning improves the reliability of biochemical signaling. *Proc. Natl. Acad. Sci. U.S.A.* **110**, 5927–5932 (2013).
11. Gillespie, D. T. The chemical langevin equation. *J. Chem. Phys.* **113**, 297–306 (2000).
12. Erban, R. & Chapman, S. J. *Stochastic Differential Equations*, 59–94 (Cambridge University Press, 2020).
13. Swain, P. S. Efficient attenuation of stochasticity in gene expression through post-transcriptional control. *J. Mol. Biol.* **344**, 965–976 (2004).

14. Alon, U. *An Introduction to Systems Biology: Design Principles of Biological Circuits* (CRC Press, Boca Raton, FL, 2006).
15. Mehta, P., Goyal, S., Long, T., Bassler, B. L. & Wingreen, N. S. Information processing and signal integration in bacterial quorum sensing. *Mol. Syst. Biol.* **5**, 325 (2009).
16. Cheong, R., Rhee, A., Wang, C. J., Nemenman, I. & Levchenko, A. Information transduction capacity of noisy biochemical signaling networks. *Science* **334**, 354–358 (2011).
17. Peyré, G. & Cuturi, M. Computational optimal transport. *Found. Trends Mach. Learn.* **11**, 355–607 (2019).